DE GRUYTER

Nanotechnology Reviews 2024; 13: 20240031

Research Article

Humaira Yasmin*, Laila A. AL-Essa, Rawan Bossly, Hussam Alrabaiah, Showkat Ahmad Lone, and Anwar Saeed*

A homotopic analysis of the blood-based bioconvection Carreau–Yasuda hybrid nanofluid flow over a stretching sheet with convective conditions

https://doi.org/10.1515/ntrev-2024-0031
received December 1, 2023; accepted April 21, 2024

Abstract: The time-independent and incompressible blood-based hybrid nanofluid flow, including Au and Cu nanoparticles across an expanding sheet, has been studied. To illustrate the non-Newtonian performance of the blood-based hybrid nanofluid flow, a non-Newtonian model known as the Carreau–Yasuda model is used. The hybrid nanofluid flow is studied under the influence of magnetic effects, thermal radiation, Brownian motion, thermophoresis, and chemical reactivity. Homotopy analysis method (HAM) is employed to evaluate the modeled equations. A study is conducted on the convergence analysis of HAM, and the HAM and numerical analyses are compared. From the present analysis, the velocity profile increases with an increase in Weissenberg number and decreases with increasing magnetic factor. The temperature, concentration, and microorganisms profiles increase in tandem with the higher thermal Biot, concentration Biot, and microorganism Biot numbers. The thermal and concentration profiles, respectively, have decreased due to the larger thermal and concentration relaxation time factors. The microorganism profiles have decreased due to the increased bioconvection of Lewis and Peclet populations. The modeled equations can be solved by both the HAM and the numerical approaches, validating both approaches to solution.

Keywords: non-Newtonian fluid, nanofluid, hybrid nanofluid, MHD, chemical reaction, motile microorganisms, convective conditions, Cattaneo-Christov heat and mass flux model

Nomenclature

Symbol

$u_{\mathrm{w}}(x)$ ($\mathrm{m\ s^{-1}}$)	stretching velocity
T (K)	temperature
C ($\mathrm{mol\ m^{-3}}$)	nanoparticle concentration
N	microorganisms concentration
μ_0	zero share stress viscosity
μ_∞	infinite share stress viscosity
Γ, D	Carreau–Yasuda liquid factors
A_1	Rivlin–Ericksen tensor
τ	shear stress
u, v ($\mathrm{m\ s^{-1}}$)	velocity components
ν ($\mathrm{m^{-2}\ s^{-1}}$)	kinematic viscosity
σ ($\mathrm{S\ m^{-1}}$)	electrical conductivity
ρ ($\mathrm{kg\ m^{-3}}$)	density
B_0 ($\mathrm{kg\ s^{-2}\ A^{-1}}$)	magnetic field strength
k ($\mathrm{W\ m^{-1}\ K^{-1}}$)	thermal conductivity
C_{p} ($\mathrm{J\ K^{-1}\ kg^{-1}}$)	specific heat
σ^* ($\mathrm{W\ m^{-2}\ K^{-4}}$)	Stefan–Boltzmann constant

*** Corresponding author: Humaira Yasmin,** Department of Basic Sciences, General Administration of Preparatory Year, King Faisal University, P.O. Box 400, Al Ahsa 31982, Saudi Arabia; Department of Mathematics and Statistics, College of Science, King Faisal University, P.O. Box 400, Al Ahsa 31982, Saudi Arabia, e-mail: hhassain@kfu.edu.sa
*** Corresponding author: Anwar Saeed,** Department of Mathematics, Abdul Wali Khan University, Mardan, 23200, Khyber Pakhtunkhwa, Pakistan, e-mail: anwarsaeed769@gmail.com
Laila A. AL-Essa: Department of Mathematical Sciences, College of Science, Princess Nourah bint Abdulrahman University, P.O. Box 84428, Riyadh 11671, Saudi Arabia
Rawan Bossly: Department of Mathematics, College of Science, Jazan University, Jazan 82817, Saudi Arabia
Hussam Alrabaiah: College of Engineering, Al Ain University, Al Ain, United Arab Emirates; Mathematics Department, Tafila Technical University, Tafila, Jordan
Showkat Ahmad Lone: Department of Basic Sciences, College of Science and Theoretical Studies, Saudi Electronic University, Jeddah-M, Riyadh 11673, Saudi Arabia

k^*	absorption coefficient
D_{B} ($\mathrm{m^{-2}\,s^{-1}}$), D_{T} ($\mathrm{m^{-2}\,s^{-1}}$)	Brownian and thermophoresis diffusion coefficients
n	power index
k_{c} ($\mathrm{s^{-1}}$)	reaction coefficient
$\tilde{\lambda}$	volume fraction of the solid nanoparticle
We	Weissenberg number
M	magnetic factor
Rd	radiation factor
Nb	Brownian motion factor
Nt	thermophoresis factor
Ec	Eckert number
Sc	Schmidt number
δ	chemical reaction factor
Pr	Prandtl number
δ_{T}	thermal relaxation time factor
δ_{C}	concentration relaxation factor
Lb, Pe	bioconvection Lewis and Peclet numbers
Ω	microorganism difference factor
$\mathrm{Bi_T}$	thermal Biot number
$\mathrm{Bi_C}$	concentration Biot number
$\mathrm{Bi_N}$	microorganism Biot number

Subscripts

hnf	hybrid nanofluid
nf	nanofluid
f	fluid
1	first nanoparticle
2	second nanoparticle

1 Introduction

Non-Newtonian fluid, unlike their Newtonian counterparts, exhibits varying viscosities under different flow circumstances, thereby influencing heat transfer processes in diverse ways. In laminar flow zones, where the viscous nature of non-Newtonian fluids can be shear-rate-dependent, the rate of heat transference is affected by the fluid's flow behavior [1]. For instance, in shear-thinning fluids like certain polymer solutions or molten plastics, viscosity decreases with increasing shear rate, promoting enhanced mixing and convective heat transfer. Conversely, shear-thickening fluids such as concentrated suspensions or certain biological fluids exhibit increased viscosity under shear, which can hinder flow and heat transfer in some scenarios [2]. Asghar *et al.* [3] studied non-Newtonian flow of the fluid on a permeable sheet with magnetic effects. Moreover, non-Newtonian fluids can also form complex flow patterns, such as vortex structures and boundary layers, which alter the distribution of heat within a system [4]. Punith Gowda *et al.* [5] inspected non-Newtonian fluid flow on an elongating surface with influences of magnetic field and chemical reactivity. Nazeer *et al.* [6] studied computationally the non-Newtonian multiphase fluid flow on an inclined conduit. In practical applications, such as chemical processing, food industry, and polymer extrusion, understanding the rheological behavior of non-Newtonian fluids is crucial for optimizing heat transfer processes, designing efficient equipment, and ensuring product quality and consistency. Additionally, in thermal management systems like microfluidic devices or the cooling of electronic components, the unique rheological properties of non-Newtonian fluids can be leveraged to tailor heat transfer characteristics for specific requirements, offering opportunities for improved energy efficiency and performance. Ragupathi and Prakash [7] studied the effects of linear and nonlinear thermal radiations on a fluid flow on gyrating permeable disks using heat sinks/sources. Thus, the study and application of non-Newtonian fluids in heat transfer processes encompass a multifaceted realm where fluid dynamics, rheology, and thermal sciences intersect, offering both challenges and opportunities for innovation and optimization. Biswal *et al.* [8] studied magneto and radiative non-Newtonian fluid flow on a nonlinearly elongated sheet.

Nanofluids are engineered colloidal suspensions consisting of nanometer-sized particles dispersed within a pure fluid. Nanofluids exhibit unique thermal properties due to the high thermal conductance of mixed nanoparticles in these fluids, as suggested first by Choi and Eastman [9]. Nanofluids, comprising nanometer-sized particles, disperse. Yasmin *et al.* [10] have discussed the peristaltic mechanism in Sisko fluid flow with double-diffusive convection and induced magnetic field. It is projected that the results of this study will help in the creation of intelligent magneto-peristaltic pumps, especially for use in drug delivery and thermal applications. Bhatti *et al.* [11] deliberated on the performance of solar energy using nanofluid flow. This increased thermal conductance facilitates more efficient conduction and convective heat transfer processes, making nanofluids promising candidates for enhancing heat exchangers, electronics cooling systems, and thermal energy storage devices. Abdelsalam and Zaher [12] studied the role of zirconium nanoparticle flow on a viscous slim. Furthermore, nanofluids exhibit tunable rheological properties, enabling tailored flow behavior to optimize heat transfer characteristics in specific applications. Acharya *et al.* [13] established that growth in a nanolayer within the nanofluid flow increased the thermal flow features to 84.61% in comparison to the diameter of the nanoparticles. Researchers have observed that as time progresses, the addition of an increased quantity of nanoparticles of distinct types into traditional fluids can enhance their thermal flow behavior, leading to the emergence of a new class of fluids identified as hybrid nanofluids. Abdelsalam *et al.* [14] studied nanofluid flow through a dual-shape annulus placed vertically with elector-osmosis. This phenomenon has sparked considerable interest and investigation within the scientific community. Hybrid nanofluids combine the advantageous properties of different types of nanoparticles with those of pure fluid, thereby potentially achieving superior thermal conductivity and heat transfer performance compared to conventional nanofluids. The impacts of the porous medium and temperature-dependent variable viscosity are considered in analyzing the magnetohydrodynamic (MHD) hybrid nanofluid flow with slip phenomenon by Khalil *et al.* [15]. It is depicted that the thermal conductivity of the base fluid was greatly enhanced by the addition of nanoparticles. This enhancement has a lot of potential applications needing efficient heat transfer, particularly in engineering systems where heat dissipation is essential. By carefully selecting and blending different nanoparticles, researchers aim to engineer hybrid nanofluids with tailored thermal properties optimized for specific applications, ranging from heat exchangers and cooling systems to thermal energy storage and renewable energy technologies. Abdelsalam and Bhatti [16] studied hybrid nanofluid flow through narrowing veins using three different configurations. The synergistic effects resulting from the combination of nanoparticles offer opportunities for enhancing heat transfer efficiency, improving system performance, and addressing challenges associated with conventional heat transfer fluids. Alshehry *et al.* [17] investigated the MHD multiphase hybrid nanofluid flow over a stretching sheet with heat transfer. To enable meaningful comparisons, quantitative parametric research is conducted to examine the impact of various physical characteristics. The findings show that, even in the presence of a magnetic field, the hybrid nanofluid displays an increased rate of heat transfer than the conventional fluid. Furthermore, the development of hybrid nanofluids opens avenues for exploring innovative approaches to thermal management and advancing the efficiency and sustainability of various industrial processes and technologies [18].

MHD is a multidisciplinary field that studies the performance of electrically conducted fluids, like ionized gases and plasmas, using magnetic effects. In MHD flows, the interaction between the fluid motion, electromagnetic fields, and thermal effects can significantly impact heat transfer processes [19]. The use of a magnetic field alters the fluid flow patterns and induces electric currents, leading to changes in the temperature distribution and heat transfer rates within the system. Prakash *et al.* [20] considered the impacts of MHD on the nanofluid flow with the effects of Ohmic heating on an elongated surface immersed in a porous medium. In certain configurations, MHD can lead to increased heat transfer rates through enhanced mixing and turbulence suppression, making it beneficial for applications like nuclear fusion reactors, liquid metal cooling systems, and industrial processes involving high-temperature fluids [21,22]. However, MHD can also introduce challenges such as flow instabilities, pressure drops, and increased electrical resistance, which may need to be addressed in the design and operation of MHD systems for optimal heat transfer performance. The interaction between MHD effects and heat transfer is crucial for harnessing the potential benefits of MHD flows while mitigating associated challenges in various engineering applications. Mahesh *et al.* [23] debated the influence of radiation on couple stress MHD fluid flow on a permeable surface with dissipative effects. Jawad [24] studied the MHD fluid flow numerically on an elongating sheet that is positioned vertically with impacts of thermal radiations. Lund *et al.* [25] studied thermally dissipative MHD fluid flow in the form of uniform streams and noticed that the thermal behavior of flow amplified with progression in the concentration of nanoparticles.

Microorganisms are tiny living organisms that are imperceptible, like bacteria and fungi. Despite their small size, microorganisms play a vital role in various flow systems and industrial applications. Fluid flow with microorganisms, also known as microbial fluid dynamics, encompasses a fascinating array of phenomena occurring in diverse environments ranging from soil and marine ecosystems to human bodies [26]. In these environments, microorganisms interact with fluid flow in complex ways, influencing nutrient transport, biofilm formation, and microbial dispersion. Kada *et al.* [27] studied the significance of microorganisms on the Williamson fluid flow. The behavior of microorganisms in fluid flow is governed by a complex relationship of physical forces, biological processes, and environmental factors [28]. Hydrodynamic forces, such as shear stress and turbulence, affect the motility, orientation, and aggregation of microorganisms, impacting their ability to colonize surfaces or disperse within the fluid. Moreover, the rheological properties of microbial suspensions, including cell density, size distribution, and extracellular polymeric substances, can alter fluid flow patterns and lead to emergent collective behaviors, like bacterial swarming and bioconvection. Doh *et al.* [29] studied mass and heat transference for fluid flow through a channel placed vertically with constraints at the boundary of the third type. The dynamics of fluid flow with microorganisms is crucial for various applications, including bioremediation, wastewater treatment, and the design of biomedical devices [30]. Advances in experimental techniques, computational modeling, and interdisciplinary research have provided insights into the complex dynamics of microbial fluid interactions, shedding light on fundamental principles governing microbial ecology and evolution in dynamic fluid environments. Waqas *et al.* [31] studied bio-convective nanofluid flow on the movable surface with impacts of microorganisms and magnetic effects. Moreover, harnessing the unique capabilities of microorganisms in fluid flow holds promise for developing innovative technologies for environmental sustainability, medical diagnostics, and bioproduction processes.

The Cattaneo–Christov heat and mass flux model is associated with Fourier's [32] and Fick's laws [33], incorporating non-local effects and accounting for finite thermal and mass propagation speeds. The Cattaneo theory [34] initially proposed adjustments to Fourier's classical heat conduction model, incorporating the effects of thermal relaxation stresses arising from the finite speed of heat propagation. Building upon this foundation, Christov [35] expanded the model by substituting partial time differentiation with the Oldroyd upper convective derivative. This modification allowed for the consideration of non-local effects, thereby enhancing the accuracy of predictions in scenarios where traditional models fall short. In this model, the main equations include time derivatives of the respective gradients, introducing a relaxation time parameter that characterizes the delay in heat or mass propagation relative to the temperature or concentration gradient. Waqas *et al.* [36] analyzed comparatively the nanofluid flow by using the impacts of the Cattaneo–Christov model on fluid flow. This model is particularly relevant in situations where the classical Fourier and Fick laws fail to accurately describe thermal and mass transport, such as in systems with high thermal gradients or non-equilibrium conditions. By considering finite propagation speeds, the Cattaneo–Christov model captures transient and non-local effects, yielding more accurate predictions of temperature and concentration distributions in complex fluid flows [37]. This model has applications in several fields, like biological tissues and porous media, as well as mass transfer in chemical reactors and environmental transport phenomena [38]. Waqas *et al.* [39] applied the Cattaneo–Christov model to simulate computationally the production of entropy for fluid flow on a surface with thermal radiation. Ramesh *et al.* [40] discussed MHD effects on mass and thermal transportation for fluid flow on a stretched sheet using the Cattaneo–Christov model.

In continuation with the stated literature, this work evaluates blood-based hybrid nanofluid flow, including Au and Cu nanoparticles, across an expanding sheet using the impacts of microorganisms. Bioconvection patterns in the fluid flow across the stretched sheet can be induced by gyrotactic microorganisms. The structured movement of microorganisms as a result of their group relationships and reaction to environmental gradients is known as bioconvection. This phenomenon has the ability to alter mixing and fluid flow patterns further. Because of the way that their movement patterns change in response to fluid flow, gyrotactic bacteria can improve fluid mixing. Increased dispersion and mixing of materials in the fluid may result from this, which may have an impact on chemical reactions, ecological interactions, and the delivery of nutrients. The temperature distribution around the stretched sheet can change when gyrotactic microorganisms are present in heat-transfer settings, including thermal boundary layers. Their motion can have an impact on the rate of heat transmission by affecting the convective heat transfer coefficient. To illustrate the non-Newtonian performance of the blood-based hybrid nanofluid flow, a non-Newtonian model known as the Carreau–Yasuda model is used. The hybrid nanofluid flow problem is formulated under the influence of thermal radiation, magnetic field, Brownian motion, thermophoresis, and chemical reaction.

2 Formulation of problem

Assume the blood-based hybrid nanofluid flow containing Cu and Au nanoparticles on an extending sheet. A two-dimensional Cartesian coordinates system, with u and v in x- and y-directions, is chosen to investigate the hybrid nanofluid flow. The sheet stretches in the x-direction $u_{\mathrm{w}}(x) = ax$ as its velocity, where a is constant. The temperature, concentration, and microorganism of the fluid, surface, and free stream are denoted by T, C, and N; $T_{\mathrm{w}}, C_{\mathrm{w}}$, and N_{w}; T_∞, C_∞, and N_∞ (see Figure 1). Furthermore, it is supposed that the $T_{\mathrm{f}} > T_{\mathrm{w}}, C_{\mathrm{f}} > C_{\mathrm{w}}$, and $N_{\mathrm{f}} > N_{\mathrm{w}}$ due to convection conditions at the sheet surface. A non-Newtonian model called Carreau–Yasuda is used to discuss the non-Newtonian behavior of the blood-based hybrid nanofluid flow. The non-Newtonian Carreau–Yasuda is defined as

$$\tau = A_1\left[((1 + \Gamma\dot{\gamma})^D)^{\left(\frac{n-1}{D}\right)}(\nabla_0 - \nabla_\infty) + \nabla_\infty\right], \tag{1}$$

where ∇_0 is the viscosity at a zero shear rate and ∇_∞ is the viscosity at an infinite share rate. Also, Γ and D are the Carreau–Yasuda liquid factors. A_1 denotes the Rivlin–Ericksen tensor while the extra stress tensor is τ. Furthermore, $A_1 = \text{grad } V + (\text{grad } V)^{\mathrm{T}}$ and $\dot{\gamma} = \left(\left(\frac{1}{2}\right)\text{trace}(A_1^2)\right)^{1/2}$.

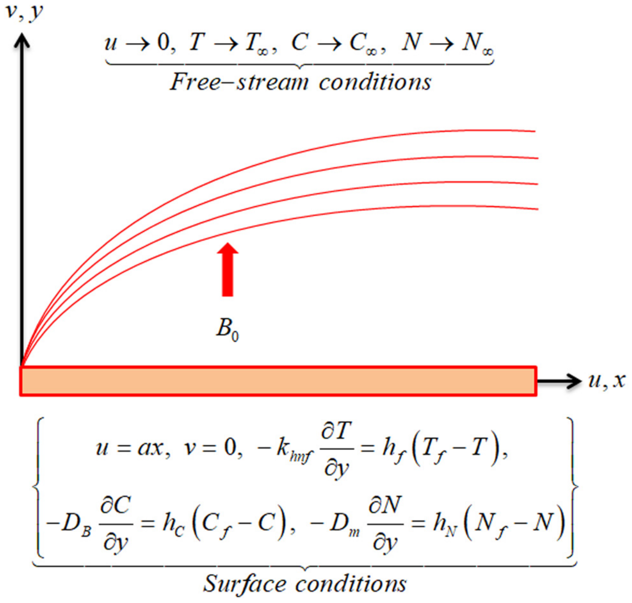

Figure 1: Geometry for the flow scheme.

For $\nabla_\infty = 0$, equation (1) is reduced to:

$$\tau = \left[\nabla_0\left(\left(1 + \Gamma\dot{\gamma}\right)^D\right)^{\left(\frac{n-1}{D}\right)}\right]A_1. \tag{2}$$

The flow behavior assumptions mentioned above generate the following equations [41,42]:

$$\frac{\partial u}{\partial x} + \frac{\partial v}{\partial y} = 0, \tag{3}$$

$$\begin{aligned} u\frac{\partial u}{\partial x} + v\frac{\partial u}{\partial y} = {} & \nu_{\mathrm{hnf}}\left(\frac{(n-1)}{D}(D+1)\Gamma^D\left(\frac{\partial u}{\partial y}\right)^D\frac{\partial^2 u}{\partial y^2}\right) \\ & + \frac{\sigma_{\mathrm{hnf}}B_0^2}{\rho_{\mathrm{hnf}}}u, \end{aligned} \tag{4}$$

$$\begin{aligned} & u\frac{\partial T}{\partial x} + v\frac{\partial T}{\partial y} + \lambda_{\mathrm{T}}\left(u^2\frac{\partial^2 T}{\partial x^2} + u\frac{\partial u}{\partial x}\frac{\partial T}{\partial x} + v\frac{\partial T}{\partial x}\frac{\partial u}{\partial y} + v^2\frac{\partial^2 T}{\partial y^2}\right. \\ & \left. + 2uv\frac{\partial^2 T}{\partial x\partial y} + u\frac{\partial T}{\partial y}\frac{\partial v}{\partial x} + v\frac{\partial v}{\partial y}\frac{\partial T}{\partial y}\right) \\ & = \left(\frac{k_{\mathrm{hnf}}}{(\rho C_{\mathrm{p}})_{\mathrm{hnf}}} + \frac{16\sigma^* T_\infty^3}{3k^*(\rho C_{\mathrm{p}})_{\mathrm{hnf}}}\right)\frac{\partial^2 T}{\partial y^2} \\ & + \frac{(\rho C_{\mathrm{p}})_{\mathrm{np}}}{(\rho C_{\mathrm{p}})_{\mathrm{hnf}}}\left(D_{\mathrm{B}}\frac{\partial T}{\partial y}\frac{\partial C}{\partial y} + \left(\frac{\partial T}{\partial y}\right)^2\left(\frac{D_{\mathrm{T}}}{T_\infty}\right)\right), \end{aligned} \tag{5}$$

$$\begin{aligned} & u\frac{\partial C}{\partial x} + v\frac{\partial C}{\partial y} + \lambda_{\mathrm{C}}\left(\begin{aligned} & u^2\frac{\partial^2 C}{\partial x^2} + v^2\frac{\partial^2 C}{\partial y^2} + \left(u\frac{\partial u}{\partial x}\frac{\partial C}{\partial x}\right. \\ & \left. + v\frac{\partial u}{\partial y}\frac{\partial C}{\partial x}\right) + 2uv\frac{\partial^2 C}{\partial x\partial y} \\ & + \left(u\frac{\partial C}{\partial y}\frac{\partial v}{\partial x} + v\frac{\partial C}{\partial y}\frac{\partial v}{\partial y}\right) \end{aligned}\right) \\ & = D_{\mathrm{B}}\frac{\partial^2 C}{\partial y^2} + \left(\frac{D_{\mathrm{T}}}{T_\infty}\right)\frac{\partial^2 T}{\partial y^2} - k_{\mathrm{c}}(C - C_\infty), \end{aligned} \tag{6}$$

$$u\frac{\partial N}{\partial x} + v\frac{\partial N}{\partial y} - D_{\mathrm{m}}\left(\frac{\partial^2 N}{\partial y^2}\right) = -\frac{bW_{\mathrm{c}}}{(C_{\mathrm{w}} - C_\infty)}\left[\frac{\partial}{\partial y}\left(N\frac{\partial C}{\partial y}\right)\right]. \tag{7}$$

With constraints at boundary,

$$\left\{\begin{aligned} & u = ax,\quad v = 0,\quad -k_{\mathrm{hnf}}\frac{\partial T}{\partial y} = h_{\mathrm{f}}(T_{\mathrm{f}} - T), \\ & -D_{\mathrm{B}}\frac{\partial C}{\partial y} = h_{\mathrm{C}}(C_{\mathrm{f}} - C), \\ & -D_{\mathrm{m}}\frac{\partial N}{\partial y} = h_{\mathrm{N}}(N_{\mathrm{f}} - N)\quad \text{at } y = 0,\ u \to 0, \\ & T \to T_\infty,\quad C \to C_\infty,\quad N \to N_\infty\quad \text{as } y \to \infty. \end{aligned}\right\} \tag{8}$$

The thermophysical features of the hybrid nanofluid can be characterized as follows with their computational values portrayed in Table 1:

$$\left\{\begin{aligned} & \frac{k_{\mathrm{hnf}}}{k_{\mathrm{f}}} = \frac{\left(\frac{\bar{\lambda}_1 k_1 + \bar{\lambda}_2 k_2}{\bar{\lambda}_1 + \bar{\lambda}_2}\right) + 2k_{\mathrm{f}} + 2(k_1\bar{\lambda}_1 + k_2\bar{\lambda}_2) - 2(\bar{\lambda}_2 + \bar{\lambda}_1)k_{\mathrm{f}}}{\left(\frac{k_1\bar{\lambda}_1 + k_2\bar{\lambda}_2}{\bar{\lambda}_1 + \bar{\lambda}_2}\right) + 2k_{\mathrm{f}} - (k_1\bar{\lambda}_1 + k_2\bar{\lambda}_2) + (\bar{\lambda}_2 + \bar{\lambda}_1)k_{\mathrm{f}}}, \\ & \rho_{\mathrm{hnf}} = (1 - (\bar{\lambda}_1 + \bar{\lambda}_2))\rho_{\mathrm{f}} + \rho_2\bar{\lambda}_2 + \bar{\lambda}_1\rho_1, \\ & \mu_{\mathrm{hnf}} = \frac{\mu_{\mathrm{f}}}{(1 - (\bar{\lambda}_2 + \bar{\lambda}_1))^{2.5}}, \\ & (\rho C_{\mathrm{p}})_{\mathrm{hnf}} = (1 - (\bar{\lambda}_2 + \bar{\lambda}_1))(\rho C_{\mathrm{p}})_{\mathrm{f}} + \bar{\lambda}_1(\rho C_{\mathrm{p}})_1 + \bar{\lambda}_2(\rho C_{\mathrm{p}})_2, \\ & \frac{\sigma_{\mathrm{hnf}}}{\sigma_{\mathrm{f}}} = \frac{\left(\frac{\bar{\lambda}_1\sigma_1 + \bar{\lambda}_2\sigma_2}{\bar{\lambda}_1 + \bar{\lambda}_2}\right) + 2\sigma_{\mathrm{f}} + 2(\bar{\lambda}_1\sigma_1 + \bar{\lambda}_2\sigma_2) - 2(\bar{\lambda}_1 + \bar{\lambda}_2)\sigma_{\mathrm{f}}}{\left(\frac{\sigma_1\bar{\lambda}_1 + \sigma_2\bar{\lambda}_2}{\bar{\lambda}_1 + \bar{\lambda}_2}\right) + 2\sigma_{\mathrm{f}} - (\sigma_1\bar{\lambda}_1 + \sigma_2\bar{\lambda}_2) + (\bar{\lambda}_2 + \bar{\lambda}_1)\sigma_{\mathrm{f}}}. \end{aligned}\right\}. \tag{9}$$

Table 1: Thermophysical features of blood, Cu, and Au [43]

Base fluid and nanoparticles	Properties			
	C_p (J/kg K)	ρ (kg/m^3)	k (W/m K)	σ (S/m)
Blood	3,594	1,063	0.492	0.667
Au	129	19,320	314	4.10×10^7
Cu	385	8,933	401	5.96×10^6

Variables for similarity are described as

$$\begin{gathered} u = axf'(\xi), \quad v = -\sqrt{a\nu_{\mathrm{f}}}\, f(\xi), \quad \phi(\xi) = \frac{C - C_{\infty}}{C_{\mathrm{f}} - C_{\infty}}, \\ \psi(\xi) = \frac{N - N_{\infty}}{N_{\mathrm{f}} - N_{\infty}}, \quad \theta(\xi) = \frac{T - T_{\infty}}{T_{\mathrm{f}} - T_{\infty}}, \quad \xi = y\sqrt{\frac{a}{\nu_{\mathrm{f}}}}. \end{gathered} \tag{10}$$

Using equation (11) in equations (3)–(8), we have

$$\begin{aligned} &\frac{\mu_{\mathrm{hnf}}}{\rho_{\mathrm{hnf}}} f'''(\xi) + \frac{\mu_{\mathrm{hnf}}}{\rho_{\mathrm{hnf}}} \frac{(n-1)}{D}(1 + D)W_{\mathrm{e}}^{\mathrm{d}}(f''(\xi))^{D} f'''(\xi) \\ &\quad + f''(\xi)f(\xi) - f'^{2}(\xi) - M\frac{\sigma_{\mathrm{hnf}}}{\rho_{\mathrm{hnf}}} f'(\xi) = 0, \end{aligned} \tag{11}$$

$$\begin{aligned} &\frac{1}{\mathrm{Pr}} \frac{1}{(\rho C_{\mathrm{p}})_{\mathrm{hnf}}/(\rho C_{\mathrm{p}})_{\mathrm{f}}} \left(\frac{k_{\mathrm{hnf}}}{k_{\mathrm{f}}} + \mathrm{Rd}\right)\theta''(\xi) \\ &\quad - \delta_{\mathrm{T}}(\theta''(\xi)f^{2}(\xi) - f'(\xi)f(\xi)\theta'(\xi)) \\ &\quad + f(\xi)\theta'(\xi) + \frac{1}{(\rho C_{\mathrm{p}})_{\mathrm{hnf}}/(\rho C_{\mathrm{p}})_{\mathrm{f}}} \{\mathrm{Nb}\theta'(\xi)\phi'(\xi) \\ &\quad + \mathrm{Nt}\theta'^{2}(\xi)\} = 0, \end{aligned} \tag{12}$$

$$\begin{aligned} &\phi''(\xi) - \mathrm{Sc}\delta_{\mathrm{C}}(f^{2}(\xi)\phi''(\xi) - f(\xi)f'(\xi)\phi'(\xi)) \\ &\quad + \mathrm{Sc}f(\xi)\phi'(\xi) + \frac{\mathrm{Nt}}{\mathrm{Nb}}\theta''(\xi) - \mathrm{Sc}\delta\phi(\xi) = 0, \end{aligned} \tag{13}$$

$$\begin{aligned} &\psi''(\xi) + \mathrm{Lb}[\psi'(\xi)f(\xi) - \psi(\xi)f'(\xi)] \\ &\quad - \mathrm{Pe}\{(\psi(\xi) + \Omega)\phi''(\xi) + \phi'(\xi)\psi'(\xi)\} = 0, \end{aligned} \tag{14}$$

The transformed constraints are

$$\left.\begin{cases} f(\xi = 0) = 0, \quad f'(\xi = 0) = 1, \quad f'(\xi \to \infty) = 0, \\ \frac{k_{\mathrm{hnf}}}{k_{\mathrm{f}}}\theta'(\xi = 0) = \mathrm{Bi}_{\mathrm{T}}\{\theta(\xi = 0) - 1\}, \quad \theta(\xi \to \infty) = 0, \\ \phi'(\xi = 0) = \mathrm{Bi}_{\mathrm{C}}\{\phi(\xi = 0) - 1\}, \quad \phi(\xi \to \infty) = 0, \\ \psi'(\xi = 0) = \mathrm{Bi}_{\mathrm{N}}\{\psi(\xi = 0) - 1\}, \quad \psi(\xi \to \infty) = 0. \end{cases}\right\} \tag{15}$$

The emerging factors appearing in the above equations are

$$\left.\begin{cases} \mathrm{We} = \frac{\sqrt{a}\, u_{\mathrm{w}}\Gamma}{\sqrt{\nu_{\mathrm{f}}}}, \quad M = \frac{\sigma_{\mathrm{f}}B_{0}^{2}}{a\rho_{\mathrm{f}}}, \quad \mathrm{Rd} = \frac{4\sigma^{*}T_{\infty}^{3}}{k_{\mathrm{f}}k^{*}}, \\ \mathrm{Nb} = \frac{(\rho C_{\mathrm{p}})_{\mathrm{np}}}{(\rho C_{\mathrm{p}})_{\mathrm{f}}} \frac{D_{\mathrm{B}}(C_{\mathrm{f}} - C_{\infty})}{\nu_{\mathrm{f}}}, \quad \mathrm{Bi}_{\mathrm{T}} = \frac{h_{\mathrm{f}}}{k_{\mathrm{f}}}\sqrt{\frac{\nu_{\mathrm{f}}}{a}}, \\ \mathrm{Nt} = \frac{(\rho C_{\mathrm{p}})_{\mathrm{np}}}{(\rho C_{\mathrm{p}})_{\mathrm{f}}} \frac{D_{\mathrm{T}}(T_{\mathrm{f}} - T_{\infty})}{\nu_{\mathrm{f}}T_{\infty}}, \\ \mathrm{Ec} = \frac{u_{w}^{2}}{(\rho C_{\mathrm{p}})_{\mathrm{f}}(T_{\mathrm{f}} - T_{\infty})}, \quad \mathrm{Sc} = \frac{\nu_{\mathrm{f}}}{D_{\mathrm{B}}}, \quad \delta = \frac{k_{\mathrm{r}}}{a}, \\ \mathrm{Bi}_{\mathrm{C}} = \frac{h_{\mathrm{C}}}{D_{\mathrm{B}}}\sqrt{\frac{\nu_{\mathrm{f}}}{a}}, \\ \mathrm{Pr} = \frac{\nu_{\mathrm{f}}(\rho C_{\mathrm{p}})_{\mathrm{f}}}{k_{\mathrm{f}}}, \quad \delta_{\mathrm{T}} = \lambda_{\mathrm{T}}a, \quad \delta_{\mathrm{C}} = \lambda_{\mathrm{C}}a, \\ \mathrm{Lb} = \frac{\nu_{\mathrm{f}}}{D_{\mathrm{m}}}, \quad \mathrm{Pe} = \frac{bW_{\mathrm{c}}}{D_{\mathrm{m}}}, \quad \Omega = \frac{N_{\infty}}{N_{\mathrm{f}} - N_{\infty}}, \\ \mathrm{Bi}_{\mathrm{N}} = \frac{h_{\mathrm{N}}}{D_{\mathrm{m}}}\sqrt{\frac{\nu_{\mathrm{f}}}{a}}. \end{cases}\right\} \tag{16}$$

The main quantities of engineering interest are described as

$$C_{\mathrm{fx}} = \frac{\tau_{\mathrm{w}}}{\rho_{\mathrm{hnf}}u_{\mathrm{w}}^{2}}, \tag{17}$$

$$\mathrm{Nu}_{x} = \frac{xq_{\mathrm{w}}}{k_{\mathrm{f}}(T_{\mathrm{f}} - T_{\infty})}, \tag{18}$$

$$\mathrm{Sh}_{x} = \frac{xq_{\mathrm{m}}}{D_{\mathrm{B}}(C_{\mathrm{f}} - C_{\infty})}, \tag{19}$$

$$\mathrm{Dn}_{x} = \frac{xq_{\mathrm{n}}}{D_{\mathrm{m}}(N_{\mathrm{f}} - N_{\infty})}, \tag{20}$$

where τ_{w}, q_{w}, q_{m}, and q_{n} are defined as

$$\tau_{\mathrm{w}} = \mu_{\mathrm{hnf}}\left\{\left(1 + \left(\frac{n-1}{D}\right)\Gamma^{D}\left(\frac{\partial u}{\partial y}\right)^{D}\right)\frac{\partial u}{\partial y}\right\}\Bigg|_{y=0}. \tag{21}$$

$$q_{\mathrm{w}} = -\left(\frac{k_{\mathrm{hnf}}}{k_{\mathrm{f}}} + \mathrm{Rd}\right)\frac{\partial T}{\partial y}\Bigg|_{y=0}. \tag{22}$$

$$q_{\mathrm{m}} = -D_{\mathrm{B}}\frac{\partial C}{\partial y}\Bigg|_{y=0}. \tag{23}$$

$$q_{\mathrm{n}} = -D_{\mathrm{m}}\frac{\partial N}{\partial y}\Bigg|_{y=0}. \tag{24}$$

Using equations (21)–(24) in equations (17)–(20), we have

$$C_{\mathrm{f}} = \frac{\mu_{\mathrm{hnf}}}{\mu_{\mathrm{f}}}\left(1 + \left(\frac{n-1}{2}\right)\mathrm{We}^{\mathrm{D}}f''^{D}(0)\right)f''(0). \tag{25}$$

$$N_{\mathrm{u}} = -\left(\frac{k_{\mathrm{hnf}}}{k_{\mathrm{f}}} + \mathrm{Rd}\right)\theta'(0). \tag{26}$$

$$S_{\mathrm{u}} = -\phi'(0). \tag{27}$$

$$n_{\mathrm{u}} = -\psi'(0). \tag{28}$$

Here, $\mathrm{Re}_{x} = \frac{u_{\mathrm{w}}x}{\nu_{\mathrm{f}}}$ is the local Reynolds number. Also, $C_{\mathrm{f}} = \sqrt{\mathrm{Re}_{x}}\,C_{\mathrm{fx}}$, $N_{\mathrm{u}} = \frac{\mathrm{Nu}_{x}}{\sqrt{\mathrm{Re}_{x}}}$, $S_{\mathrm{u}} = \frac{\mathrm{Sh}_{x}}{\sqrt{\mathrm{Re}_{x}}}$, and $n_{\mathrm{u}} = \frac{\mathrm{Dn}_{x}}{\sqrt{\mathrm{Re}_{x}}}$.

3 Homotopic approach

In order to introduce the homotopic solution, we have defined the following initial guesses:

$$\begin{gathered} f_{0}(\xi) = 1 - \exp(-\xi), \quad \theta_{0}(\xi) = \frac{\mathrm{Bi}_{\mathrm{T}}}{A_{5} + \mathrm{Bi}_{\mathrm{T}}}\exp(-\xi), \\ \phi_{0}(\xi) = \frac{\mathrm{Bi}_{\mathrm{C}}}{1 + \mathrm{Bi}_{\mathrm{C}}}\exp(-\xi), \quad \psi_{0}(\xi) = \frac{\mathrm{Bi}_{\mathrm{N}}}{1 + \mathrm{Bi}_{\mathrm{N}}}\exp(-\xi). \end{gathered} \tag{29}$$

The operators in linear form are given as

$$\begin{aligned} L_{\mathrm{f}}(\xi) &= f'''(\xi) - f'(\xi), \quad L_\theta(\xi) = \theta''(\xi) - \theta(\xi),\\ L_\phi(\xi) &= \phi''(\xi) - \phi(\xi), \quad L_\psi(\xi) = \psi''(\xi) - \psi(\xi), \end{aligned} \tag{30}$$

with the following properties:

$$\begin{aligned} &L_f(\chi_1 + \chi_2\exp(-\xi) + \chi_3\exp(\xi)) = 0,\\ &L_\theta(\chi_4\exp(-\xi) + \chi_5\exp(\xi)) = 0,\\ &L_\phi(\chi_6\exp(-\xi) + \chi_7\exp(\xi)) = 0,\\ &L_\psi(\chi_8\exp(-\xi) + \chi_9\exp(\xi)) = 0, \end{aligned} \tag{31}$$

where $\chi_z(z = 1, \ldots ,9)$ are constants of a general solution. The zeroth-order deformations are as follows:

$$(1 - P_{\mathfrak{R}})L_f[f(\xi;P_{\mathfrak{R}}),\ f_0(\xi)] = P_{\mathfrak{R}}\hbar_f N_f[f(\xi;P_{\mathfrak{R}})], \tag{32}$$

$$\begin{aligned} &(1 - P_{\mathfrak{R}})L_\theta[\theta(\xi;P_{\mathfrak{R}}), \theta_0(\xi)]\\ &\quad = P_{\mathfrak{R}}\hbar_\theta N_\theta[\theta(\xi;P_{\mathfrak{R}}), f(\xi;P_{\mathfrak{R}}), \phi(\xi;P_{\mathfrak{R}})], \end{aligned} \tag{33}$$

$$\begin{aligned} &(1 - P_{\mathfrak{R}})L_\phi[\phi(\xi;P_{\mathfrak{R}}),\ \phi_0(\xi)] = P_{\mathfrak{R}}\hbar_\phi N_\phi[\phi(\xi;P_{\mathfrak{R}}),\\ &f(\xi;P_{\mathfrak{R}}),\ \theta(\xi;P_{\mathfrak{R}})], \end{aligned} \tag{34}$$

$$\begin{aligned} &(1 - P_{\mathfrak{R}})L_\psi[\psi(\xi;P_{\mathfrak{R}}),\ \psi_0(\xi)] = P_{\mathfrak{R}}\hbar_\psi N_\psi[\psi(\xi;P_{\mathfrak{R}}),\\ &f(\xi;P_{\mathfrak{R}}), \phi(\xi;P_{\mathfrak{R}})], \end{aligned} \tag{35}$$

with boundary conditions

$$f(\xi = 0;P_{\mathfrak{R}}) = 0, \quad f'(\xi = 0;P_{\mathfrak{R}}) = 1, \quad f'(\xi \to \infty;P_{\mathfrak{R}}) = 0. \tag{36}$$

$$\begin{aligned} &\frac{k_{\mathrm{hnf}}}{k_{\mathrm{f}}}\theta'(\xi = 0;P_{\mathfrak{R}}) = \mathrm{Bi}_{\mathrm{T}}\{\theta(\xi = 0;P_{\mathfrak{R}}) - 1\},\\ &\theta(\xi \to \infty;P_{\mathfrak{R}}) = 0. \end{aligned} \tag{37}$$

$$\begin{aligned} &\phi'(\xi = 0;P_{\mathfrak{R}}) = \mathrm{Bi}_{\mathrm{C}}\{\phi(\xi = 0;P_{\mathfrak{R}}) - 1\},\\ &\phi(\xi \to \infty;P_{\mathfrak{R}}) = 0. \end{aligned} \tag{38}$$

$$\begin{aligned} &\psi'(\xi = 0;P_{\mathfrak{R}}) = \mathrm{Bi}_{\mathrm{N}}\{\psi(\xi = 0;P_{\mathfrak{R}}) - 1\},\\ &\psi(\xi \to \infty;P_{\mathfrak{R}}) = 0. \end{aligned} \tag{39}$$

The nonlinear operators are defined as

$$N_f[f(\xi;P_{\mathfrak{R}})] = \left\{\begin{aligned} &\frac{\mu_{\mathrm{hnf}}}{\rho_{\mathrm{hnf}}}\frac{\partial^3 f(\xi;P_{\mathfrak{R}})}{\partial\xi^3} + \frac{\mu_{\mathrm{hnf}}}{\rho_{\mathrm{hnf}}}\frac{(n-1)}{D}(D\\ &\quad + 1)W_{\mathrm{e}}^{\mathrm{d}}\left(\frac{\partial^2 f(\xi;P_{\mathfrak{R}})}{\partial\xi^2}\right)^D\frac{\partial^3 f(\xi;P_{\mathfrak{R}})}{\partial\xi^3}\\ &\quad + \frac{\partial^2 f(\xi;P_{\mathfrak{R}})}{\partial\xi^2}f(\xi;P_{\mathfrak{R}}) - \left(\frac{\partial f(\xi;P_{\mathfrak{R}})}{\partial\xi}\right)^2\\ &\quad - M\frac{\sigma_{\mathrm{hnf}}}{\rho_{\mathrm{hnf}}}\frac{\partial f(\xi;P_{\mathfrak{R}})}{\partial\xi} \end{aligned}\right], \tag{40}$$

$$N_\theta\begin{bmatrix}\theta(\xi;P_{\mathfrak{R}}),\\ f(\xi;P_{\mathfrak{R}}),\\ \phi(\xi;P_{\mathfrak{R}})\end{bmatrix} = \left\{\begin{aligned} &\frac{1}{\Pr}\frac{1}{(\rho C_{\mathrm{p}})_{\mathrm{hnf}}/(\rho C_{\mathrm{p}})_{\mathrm{f}}}\left(\frac{k_{\mathrm{hnf}}}{k_{\mathrm{f}}} + \mathrm{Rd}\right)\frac{\partial^2\theta(\xi;P_{\mathfrak{R}})}{\partial\xi^2}\\ &\quad + f(\xi;P_{\mathfrak{R}})\frac{\partial\theta(\xi;P_{\mathfrak{R}})}{\partial\xi}\\ &\quad -\delta_{\mathrm{T}}\Bigg(\frac{\partial^2\theta(\xi;P_{\mathfrak{R}})}{\partial\xi^2}(f(\xi;P_{\mathfrak{R}}))^2\\ &\quad - f(\xi;P_{\mathfrak{R}})\frac{\partial\theta(\xi;P_{\mathfrak{R}})}{\partial\xi}\frac{\partial f(\xi;P_{\mathfrak{R}})}{\partial\xi}\Bigg)\\ &\quad + \frac{1}{(\rho C_{\mathrm{p}})_{\mathrm{hnf}}/(\rho C_{\mathrm{p}})_{\mathrm{f}}}\Bigg\{\mathrm{Nb}\frac{\partial\phi(\xi;P_{\mathfrak{R}})}{\partial\xi}\frac{\partial\theta(\xi;P_{\mathfrak{R}})}{\partial\xi}\\ &\quad + \mathrm{Nt}\left(\frac{\partial\theta(\xi;P_{\mathfrak{R}})}{\partial\xi}\right)^2\Bigg\} \end{aligned}\right], \tag{41}$$

$$N_\phi\begin{bmatrix}\phi(\xi;P_{\mathfrak{R}}),\\ \theta(\xi;P_{\mathfrak{R}}),\ f(\xi;P_{\mathfrak{R}})\end{bmatrix} = \left\{\begin{aligned} &-\mathrm{Sc}\delta_{\mathrm{C}}\Bigg((f(\xi;P_{\mathfrak{R}}))^2\frac{\partial^2\phi(\xi;P_{\mathfrak{R}})}{\partial\xi^2}\\ &\quad - f(\xi;P_{\mathfrak{R}})\frac{\partial\phi(\xi;P_{\mathfrak{R}})}{\partial\xi}\frac{\partial f(\xi;P_{\mathfrak{R}})}{\partial\xi}\Bigg)\\ &\quad + \frac{\partial^2\phi(\xi;P_{\mathfrak{R}})}{\partial\xi^2} + \mathrm{Sc}\frac{\partial\phi(\xi;P_{\mathfrak{R}})}{\partial\xi}f(\xi;P_{\mathfrak{R}})\\ &\quad + \frac{\mathrm{Nt}}{\mathrm{Nb}}\frac{\partial^2\theta(\xi;P_{\mathfrak{R}})}{\partial\xi^2} - \mathrm{Sc}\delta\phi(\xi;P_{\mathfrak{R}}) \end{aligned}\right], \tag{42}$$

$$N_\psi\begin{bmatrix}\psi(\xi;P_{\mathfrak{R}}),\\ \phi(\xi;P_{\mathfrak{R}}),\ f(\xi;P_{\mathfrak{R}})\end{bmatrix} = \left\{\begin{aligned} &\frac{\partial^2\psi(\xi;P_{\mathfrak{R}})}{\partial\xi^2} + \mathrm{Lb}\Bigg[f(\xi;P_{\mathfrak{R}})\frac{\partial\psi(\xi;P_{\mathfrak{R}})}{\partial\xi}\\ &\quad - \psi(\xi;P_{\mathfrak{R}})\frac{\partial f(\xi;P_{\mathfrak{R}})}{\partial\xi}\Bigg]\\ &\quad - \mathrm{Pe}\Bigg\{\frac{\partial^2\phi(\xi;P_{\mathfrak{R}})}{\partial\xi^2}(\Omega + \psi(\xi;P_{\mathfrak{R}}))\\ &\quad + \frac{\partial\phi(\xi;P_{\mathfrak{R}})}{\partial\xi}\frac{\partial\psi(\xi;P_{\mathfrak{R}})}{\partial\xi}\Bigg\} \end{aligned}\right], \tag{43}$$

where $P_{\mathfrak{R}} \in [0\,1]$ and $\hbar_f$, $\hbar_\theta$, $\hbar_\phi$, and $\hbar_\psi$ are the embedding factors.

The mth-order deformations are as follows:

$$L_f[f_m(\xi) - \varpi_m f_{m-1}(\xi)] = \hbar_f R_m^f(\xi), \tag{44}$$

$$L_\theta[\theta_m(\xi) - \varpi_m\theta_{m-1}(\xi)] = \hbar_\theta R_m^\theta(\xi), \tag{45}$$

$$L_{\phi}[\phi_m(\xi) - \varpi_m\phi_{m-1}(\xi)] = \hbar_{\phi}R_m^{\phi}(\xi), \tag{46}$$

$$L_{\psi}[\psi_m(\xi) - \varpi_m\psi_{m-1}(\xi)] = \hbar_{\psi}R_m^{\psi}(\xi). \tag{47}$$

with constraints as

$$f_m(\xi = 0) = f'_m(\xi = 0) = f'(\xi = \infty) = 0, \tag{48}$$

$$\frac{k_{\mathrm{hnf}}}{k_{\mathrm{f}}}\theta'_m(\xi = 0) - \mathrm{Bi}_{\mathrm{T}}\{\theta_m(\xi = 0) - 1\} = \theta_m(\xi = \infty) = 0, \tag{49}$$

$$\phi'_m(\xi = 0) - \mathrm{Bi}_{\mathrm{C}}\{\phi_m(\xi = 0) - 1\} = \phi(\xi = \infty) = 0, \tag{50}$$

$$\psi'_m(\xi = 0) - \mathrm{Bi}_{\mathrm{N}}\{\psi_m(\xi = 0) - 1\} = \psi_m(\xi = \infty) = 0, \tag{51}$$

$$R_m^f(\xi) = \left\{\begin{array}{l} \dfrac{\mu_{\mathrm{hnf}}}{\rho_{\mathrm{hnf}}}f'''_{m-1}(\xi) + \dfrac{\mu_{\mathrm{hnf}}}{\rho_{\mathrm{hnf}}}\dfrac{(n-1)}{D}(D \\ \quad + 1)W_{\mathrm{e}}^{\mathrm{d}}(f''_{m-1}(\xi))^{\mathrm{D}}f'''_{m-1}(\xi) \\ \quad + \displaystyle\sum_{k=0}^{m-1} f_{m-1-k}(\xi)f''_m(\xi) - \sum_{k=0}^{m-1} f'_{m-1-k}(\xi)f'_m(\xi) \\ \quad - M\dfrac{\sigma_{\mathrm{hnf}}}{\rho_{\mathrm{hnf}}}f'_{m-1}(\xi) \end{array}\right\}, \tag{52}$$

$$R_m^{\theta}(\xi) = \left\{\begin{array}{l} \dfrac{1}{\mathrm{Pr}}\dfrac{1}{(\rho C_{\mathrm{p}})_{\mathrm{hnf}}/(\rho C_{\mathrm{p}})_{\mathrm{f}}}\left(\dfrac{k_{\mathrm{hnf}}}{k_{\mathrm{f}}} + \mathrm{Rd}\right)\theta''_{m-1}(\xi) \\ \quad + \displaystyle\sum_{k=0}^{m-1} f_{m-1-k}(\xi)\theta'_m(\xi) \\ \quad - \delta_{\mathrm{T}}\left\{\displaystyle\sum_{k=0}^{m-1} f_{m-1-k}(\xi)\sum_{l=0}^{k} f_{k-l}(\xi)\theta''_m(\xi) \right. \\ \quad \left. - \displaystyle\sum_{k=0}^{m-1} f_{m-1-k}(\xi)\sum_{l=0}^{k} f'_{k-l}(\xi)\theta'_m(\xi)\right\} \\ \quad + \dfrac{1}{(\rho C_{\mathrm{p}})_{\mathrm{hnf}}/(\rho C_{\mathrm{p}})_{\mathrm{f}}}\left\{\mathrm{Nb}\displaystyle\sum_{k=0}^{m-1} \phi'_{m-1-k}(\xi)\theta'_m(\xi) \right. \\ \quad \left. + \mathrm{Nt}\displaystyle\sum_{k=0}^{m-1} \theta'_{m-1-k}(\xi)\theta'_m(\xi)\right\} \end{array}\right\}, \tag{53}$$

$$R_m^{\phi}(\xi) = \left\{\begin{array}{l} \phi''_{m-1}(\xi) + \mathrm{Sc}\displaystyle\sum_{k=0}^{m-1} f_{k-1-m}(\xi)\phi'_m(\xi) + \dfrac{\mathrm{Nt}}{\mathrm{Nb}}\theta''_{m-1}(\xi) \\ \quad - \mathrm{Sc}\delta\phi_{m-1}(\xi) \\ \quad - \mathrm{Sc}\delta_{\mathrm{C}}\left\{\displaystyle\sum_{k=0}^{m-1} f_{m-1-k}(\xi)\sum_{l=0}^{k} f_{k-l}(\xi)\phi''_m(\xi) \right. \\ \quad \left. - \displaystyle\sum_{k=0}^{m-1} f_{m-1-k}(\xi)\sum_{l=0}^{k} f'_{k-l}(\xi)\phi'_m(\xi)\right\} \end{array}\right\}, \tag{54}$$

$$R_m^{\psi}(\xi) = \left\{\begin{array}{l} \psi''_{m-1}(\xi) + \mathrm{Lb}\left[\displaystyle\sum_{k=0}^{m-1} f_{k-1-m}(\xi)\psi'_m(\xi) \right. \\ \quad \left. - \displaystyle\sum_{k=0}^{m-1} f'_{k-1-m}(\xi)\psi_m(\xi)\right] \\ \quad - \mathrm{Pe}\left\{\displaystyle\sum_{k=0}^{m-1} \psi_m(\xi)\phi''_{k-1-m}(\xi) + \Omega\phi''_{m-1}(\xi) \right. \\ \quad \left. + \displaystyle\sum_{k=0}^{m-1} \phi'_{k-1-m}(\xi)\psi'_m(\xi)\right\} \end{array}\right\}. \tag{55}$$

For $P_{\mathfrak{R}} = 1$ and $P_{\mathfrak{R}} = 0$, we can write

$$f(\xi;0) = f_0(\xi), \quad f(\xi;1) = f(\xi), \tag{56}$$

$$\theta(\xi;0) = \theta_0(\xi), \quad \theta(\xi;1) = \theta(\xi), \tag{57}$$

$$\phi(\xi;0) = \phi_0(\xi), \quad \phi(\xi;1) = \phi(\xi). \tag{58}$$

$$\psi(\xi;0) = \psi_0(\xi), \quad \psi(\xi;1) = \psi(\xi). \tag{59}$$

When $P_{\mathfrak{R}}$ varies from 0 to 1, then $f(\xi\, ;P_{\mathfrak{R}})$, $\theta(\xi\, ;\, P_{\mathfrak{R}})$, $\phi(\xi;P_{\mathfrak{R}})$, and $\psi(\xi\, ;\, P_{\mathfrak{R}})$ vary from initial to final solutions. Using Taylor series expansion, we have

$$\begin{aligned} f(\xi;P_{\mathfrak{R}}) &= f_0(\xi) + \sum_{m=1}^{\infty} f_m(\xi)P_{\mathfrak{R}}^m, \\ f_m(\xi) &= \frac{1}{m!}\frac{\partial^m f(\xi;P_{\mathfrak{R}})}{\partial P_{\mathfrak{R}}^m}\Bigg|_{P_{\mathfrak{R}}=0}, \end{aligned} \tag{60}$$

$$\begin{aligned} \theta(\xi;P_{\mathfrak{R}}) &= \theta_0(\xi) + \sum_{m=1}^{\infty} \theta_m(\xi)P_{\mathfrak{R}}^m, \\ \theta_m(\xi) &= \frac{1}{m!}\frac{\partial^m \theta(\xi;P_{\mathfrak{R}})}{\partial P_{\mathfrak{R}}^m}\Bigg|_{P_{\mathfrak{R}}=0}, \end{aligned} \tag{61}$$

$$\begin{aligned} \phi(\xi;P_{\mathfrak{R}}) &= \phi_0(\xi) + \sum_{m=1}^{\infty} \phi_m(\xi)P_{\mathfrak{R}}^m, \\ \phi_m(\xi) &= \frac{1}{m!}\frac{\partial^m \phi(\xi;P_{\mathfrak{R}})}{\partial P_{\mathfrak{R}}^m}\Bigg|_{P_{\mathfrak{R}}=0}, \end{aligned} \tag{62}$$

$$\begin{aligned} \psi(\xi;P_{\mathfrak{R}}) &= \psi_0(\xi) + \sum_{m=1}^{\infty} \psi_m(\xi)P_{\mathfrak{R}}^m, \\ \psi_m(\xi) &= \frac{1}{m!}\frac{\partial^m \psi(\xi;P_{\mathfrak{R}})}{\partial P_{\mathfrak{R}}^m}\Bigg|_{P_{\mathfrak{R}}=0}, \end{aligned} \tag{63}$$

At $P_{\mathfrak{R}} = 1$, the above series (60)–(63) converge, *i.e.*

$$f(\xi) = \sum_{m=1}^{\infty} f_m(\xi) + f_0(\xi). \tag{64}$$

$$\theta(\xi) = \sum_{m=1}^{\infty} \theta_m(\xi) + \theta_0(\xi). \tag{65}$$

$$\phi(\xi) = \sum_{m=1}^{\infty} \phi_m(\xi) + \phi_0(\xi). \tag{66}$$

$$\psi(\xi) = \psi_0(\xi) + \sum_{m=1}^{\infty} \psi_m(\xi). \tag{67}$$

4 Convergence of HAM

Homotopy analysis method (HAM) ensures the convergence of a series of solutions. The factor $\hbar$ plays an important role in regulating the convergence area of the solution in series. Figure 2(a)–(d) is used to determine the convergence of velocity $f'(\xi)$, temperature $\theta(\xi)$, concentration $\phi(\xi)$, and microorganism $\psi(\xi)$ profiles. From these figures, we determined that the convergence area at the 15th-order approximation is $-1.2 \le \hbar_f \le 0.5$ for the velocity, $-1.5 \le \hbar_\theta \le 0.3$ for the temperature panels, $-1.5 \le \hbar_\phi \le 0.28$ for the concentration panels, and $-1.5 \le \hbar_\psi \le 0.28$ for the microorganism profiles.

5 HAM and numerical comparison

This section presents the matching of HAM and numerical methods for velocity $f'(\xi)$, temperature $\theta(\xi)$, concentration $\phi(\xi)$, and microorganism $\psi(\xi)$ profiles. The HAM technique is conducted at 15th-order approximation and then compared with numerical techniques. The results of both HAM and numerical methods are presented in Tables 2–5 and Figure 3(a)–(d). From these tables and figures, we have proven that both the HAM and numerical methods solve the modeled equations, which validates both the solution methodologies.

6 Discussion

Figure 4 shows the impact of (M) on $f'(\xi)$: increasing M decreases $f'(\xi)$. Essentially, the Lorentz forces are formed at higher M, which opposes the fluid velocity. This opposing force, due to the Lorentz force, enhances the friction force

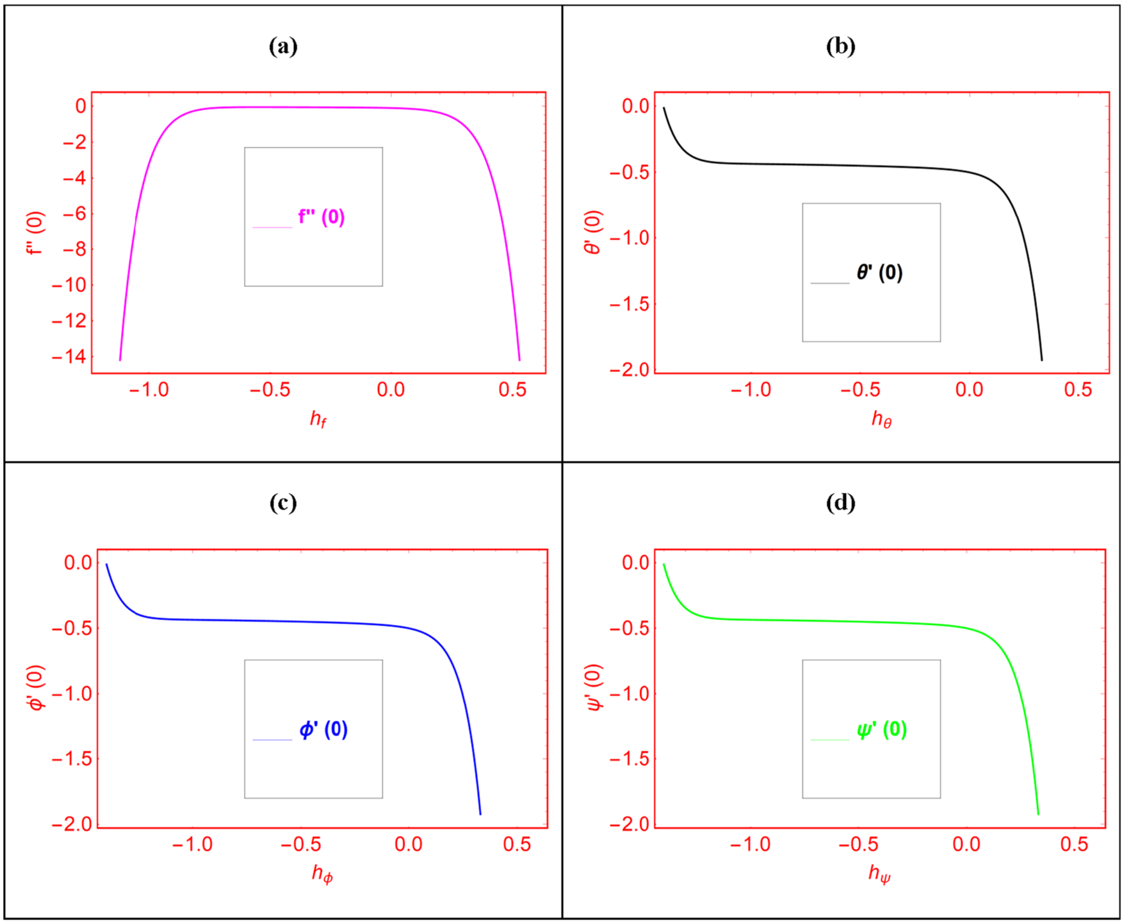

Figure 2: (a)–(d) $\hbar$ curves for $f''(0)$, $\theta'(0)$, $\phi'(0)$, and $\psi'(0)$.

Table 2: HAM *vs* numerical solution for $f'(\xi)$

ξ	$f'(\xi)$		
	HAM solution	**Numerical solution**	**|HAM – numerical|**
0.0	1.0	1.0	0.0
0.5	0.6136901962688692	0.6136822412282511	$7.95504061812391 \times 10^{-6}$
1.0	0.3748557659094872	0.3748480144375560	$7.75147193116110 \times 10^{-6}$
1.5	0.2283304529018467	0.2283246747987874	$5.77810305935067 \times 10^{-6}$
2.0	0.1388458725670490	0.1388419719122374	$3.90065481162271 \times 10^{-6}$
2.5	0.0843454101726432	0.0843428986042557	$2.51156838748656 \times 10^{-6}$
3.0	0.0512063178535998	0.0512047409097268	$1.57694387303841 \times 10^{-6}$
3.5	0.0310759484660214	0.0310749722826395	$9.76183381892755 \times 10^{-7}$
4.0	0.0188550441765591	0.0188544448373504	$5.99339208692817 \times 10^{-7}$
4.5	0.0114385641402669	0.0114381979540425	$3.66186224471515 \times 10^{-7}$
5.0	0.0069387234111651	0.0069385003262628	$2.23084902310592 \times 10^{-7}$
5.5	0.0042088735305942	0.0042087378616030	$1.356689912556815 \times 10^{-7}$
6.0	0.0025529304155957	0.0025528479953302	$8.242026547713989 \times 10^{-8}$

Table 3: HAM *vs* numerical solution for $\theta(\xi)$

ξ	$\theta(\xi)$		
	HAM solution	**Numerical solution**	**|HAM – numerical|**
0.0	0.4731921487603305	0.4731920548545173	$9.39058132365389 \times 10^{-8}$
0.5	0.2806483026704129	0.2806482259117134	$7.67586995076289 \times 10^{-8}$
1.0	0.1682851385238433	0.1682850875489276	$5.09749157329535 \times 10^{-8}$
1.5	0.1014473447866921	0.1014473128829621	$3.19037300328177 \times 10^{-8}$
2.0	0.0613218438290716	0.0613218242585015	$1.95705701505683 \times 10^{-8}$
2.5	0.0371211279766323	0.0371211160573974	$1.19192349393175 \times 10^{-8}$
3.0	0.0224894457738898	0.0224894385335563	$7.24033357921195 \times 10^{-9}$
3.5	0.0136313222557260	0.0136313178617980	$4.39392805473556 \times 10^{-9}$
4.0	0.0082644740725819	0.0082644714069845	$2.66559735742633 \times 10^{-9}$
4.5	0.0050114389675497	0.0050114373506615	$1.61688819191180 \times 10^{-9}$
5.0	0.0030391457967907	0.0030391448160713	$9.8071940889469 \times 10^{-10}$
5.5	0.0018431717342258	0.0018431711393834	$5.9484244786808 \times 10^{-10}$
6.0	0.0011178801901255	0.0011178798293340	$3.6079153380164 \times 10^{-10}$

Table 4: HAM *vs* numerical solution for $\phi(\xi)$

ξ	$\phi(\xi)$		
	HAM solution	**Numerical solution**	**|HAM – numerical|**
0.0	0.3150925925925926	0.3150870398134266	$5.55277916597324 \times 10^{-6}$
0.5	0.1846265939364708	0.1846212382393886	$5.35569708214425 \times 10^{-6}$
1.0	0.1096207934773012	0.1096168138244716	$3.97965282955548 \times 10^{-6}$
1.5	0.0656255225196950	0.0656228397233275	$2.68279636748966 \times 10^{-6}$
2.0	0.0394877332036752	0.0394860070403693	$1.72616330589882 \times 10^{-6}$
2.5	0.0238344953145856	0.0238334119364077	$1.08337817751951 \times 10^{-6}$
3.0	0.0144137318001615	0.0144130613046167	$6.70495544740267 \times 10^{-7}$
3.5	0.0087267051692205	0.0087262935659354	$4.11603286650856 \times 10^{-7}$
4.0	0.0052872545184834	0.0052870030558631	$2.51462620245636 \times 10^{-7}$
4.5	0.0032047637871987	0.0032046106005885	$1.53186610248196 \times 10^{-7}$
5.0	0.0019430084140240	0.0019429152563384	$9.31576856184056 \times 10^{-8}$
5.5	0.0011782076025241	0.0011781510092871	$5.65932369677481 \times 10^{-8}$
6.0	0.0007145136180279	0.0007144792592955	$3.43587324906354 \times 10^{-8}$

Table 5: HAM *vs* numerical solution for $\psi(\xi)$

ξ	$\psi(\xi)$		
	HAM solution	**Numerical solution**	**|HAM – numerical|**
0.0	0.33410437710437707	0.3341088269287378	$4.44982436008288 \times 10^{-6}$
0.5	0.20291700716968594	0.2029197098537764	$2.70268409044274 \times 10^{-6}$
1.0	0.12317351610064704	0.1231751567052734	$1.64060462643538 \times 10^{-6}$
1.5	0.07474414488862194	0.0747451404537535	$9.95565131611806 \times 10^{-7}$
2.0	0.04534761872759574	0.0453482227465475	$6.04018951827489 \times 10^{-7}$
2.5	0.02750948136719789	0.0275098477884470	$3.66421249158721 \times 10^{-7}$
3.0	0.01668708987451511	0.0166873121441665	$2.22269651437676 \times 10^{-7}$
3.5	0.01012187278235457	0.0101220076045005	$1.34822145964695 \times 10^{-7}$
4.0	0.00613946178345131	0.0061395435604457	$8.17769944729673 \times 10^{-8}$
4.5	0.00372385842297197	0.0037239080244136	$4.96014416415113 \times 10^{-8}$
5.0	0.00225866615772337	0.0022586962429550	$3.00852317082316 \times 10^{-8}$
5.5	0.00136996198944089	0.0013699802372169	$1.82477760854463 \times 10^{-8}$
6.0	0.00083092825820074	0.0008309393260954	$1.10678946837554 \times 10^{-8}$

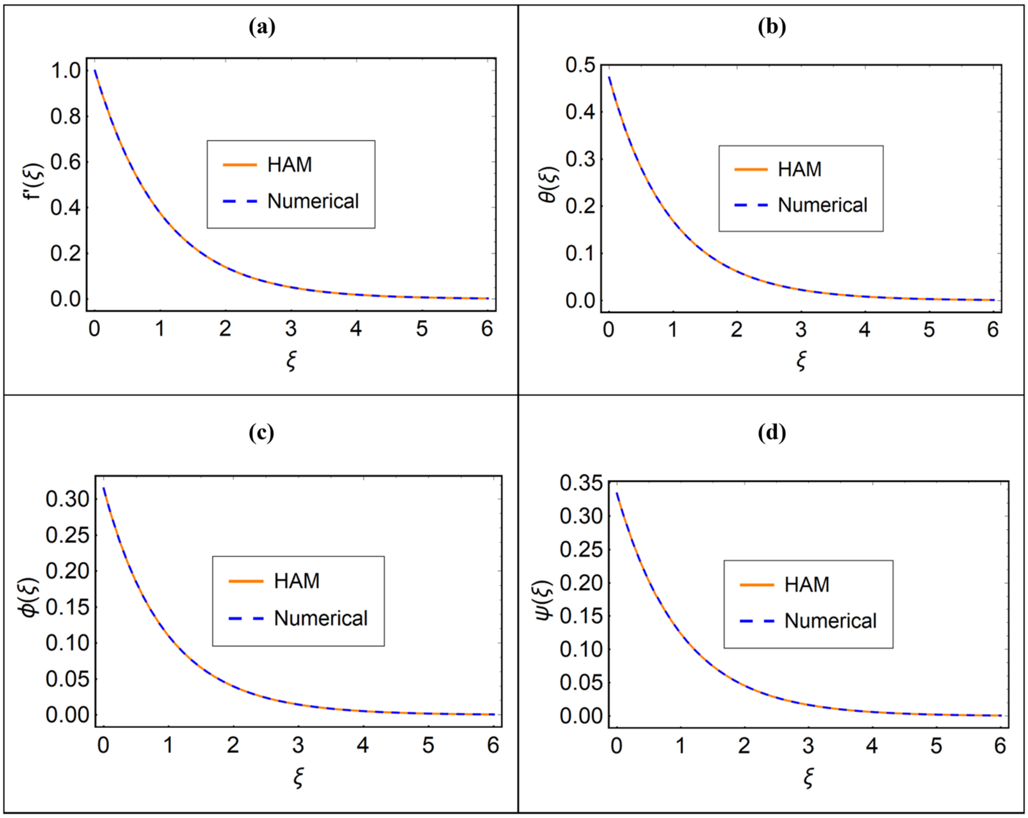

Figure 3: (a)–(d) HAM and numerical comparisons for $f'(\xi)$, $\theta(\xi)$, $\phi(\xi)$, and $\psi(\xi)$.

on the sheet's surface, which results in decreasing the hybrid nanofluid flow velocity. Figure 5 shows the effect of Weissenberg number (We) on $f'(\xi)$. It is found the increasing We increases $f'(\xi)$. The Weissenberg number is actually the ratio of elastic to resistive forces. In fact, the fluid elasticity increases when We exceeds the relaxation time of the hybrid nanofluid particles, which causes the particles to slow down. This action leads to an improvement in the velocity outline. Figure 6 shows the impact of thermal Biot number $\mathrm{Bi_T}$ on $\theta(\xi)$. It is found that an increase in $\mathrm{Bi_T}$ increases $\theta(\xi)$. Convective heat transmission is more important than conductive heat transfer when $\mathrm{Bi_T}$ increases. When the convective heat

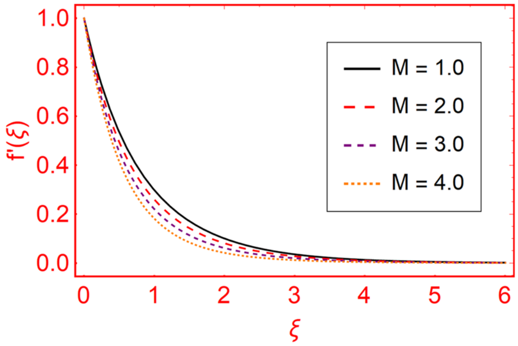

Figure 4: Impact of M on $f'(\xi)$.

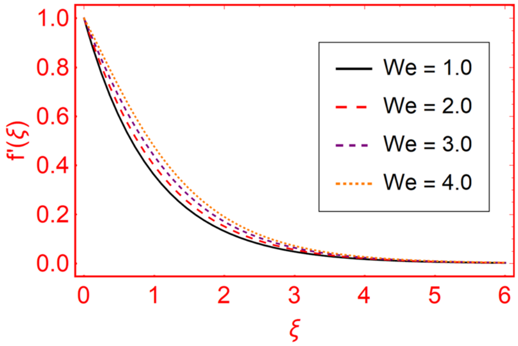

Figure 5: Impact of We on $f'(\xi)$.

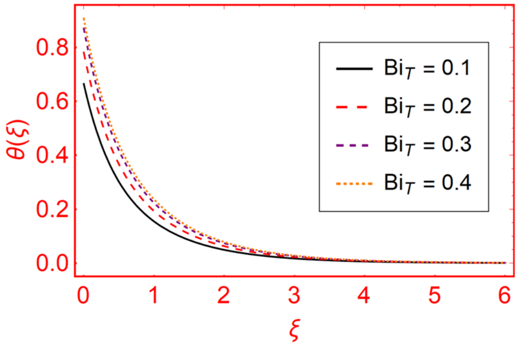

Figure 6: Impact of Bi_T on $\theta(\xi)$.

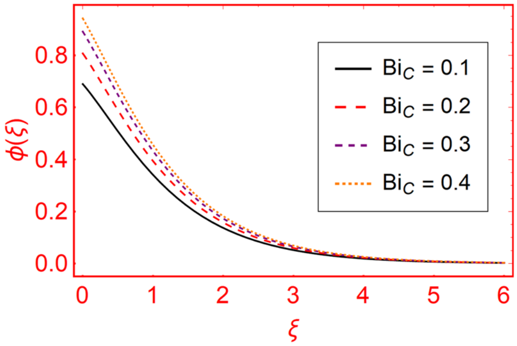

Figure 7: Impact of Bi_C on $\phi(\xi)$.

transfer coefficient increases, this frequently happens. Convective heat transmission overtakes conductive heat transfer in situations when Bi_T is higher. As a result, the temperature gradient near the surface increases, raising the thermal panels of the fluid flowing across the expanding surface. Figure 7 shows the impact of the concentration Biot number Bi_C on $\phi(\xi)$. It is found that increasing Bi_C enhances $\phi(\xi)$. The higher Bi_C increases the concentration gradient close to the surface, raising the concentration profile of the fluid flowing across the expanding surface. Figure 8 shows the impact of the microorganism Biot number Bi_N on $\psi(\xi)$. It is found that increasing Bi_N enhances $\psi(\xi)$. The higher Bi_N increases the concentration gradient close to the surface, raising the microorganism profile of the fluid flowing across the expanding surface. Figure 9 depicts the effect of the temperature relaxation time factor (δ_T) on $\theta(\xi)$. From this figure, it is found that the larger δ_T decreases $\theta(\xi)$. The relationship between thermal distribution and thermal relaxation parameters is affected. The analysis also shows that the width of the thermal layer at the frontiers diminishes. Basically, the particles of materials require more time to convey heat to their nearby particles as δ_T increase. In other words, we may state that a material exhibits non-conducting characteristics at larger values of δ_T, which decreases $\theta(\xi)$. Figure 10 shows the effect of the concentration relaxation time factor (δ_C) on $\phi(\xi)$. From this figure, it is found that higher δ_C reduces $\phi(\xi)$. The relationship between concentration distribution and concentration relaxation parameter is affected. The analysis also shows that the width of the concentration layer at frontiers diminishes. It is because the particles of the material require large time to transmit mass to their nearby particles as δ_C increases. In other words, we may state that a material exhibits non-conducting characteristics at larger values of δ_C, which decreases the concentration distribution. With progression in (Nb) there is a corresponding increase in the

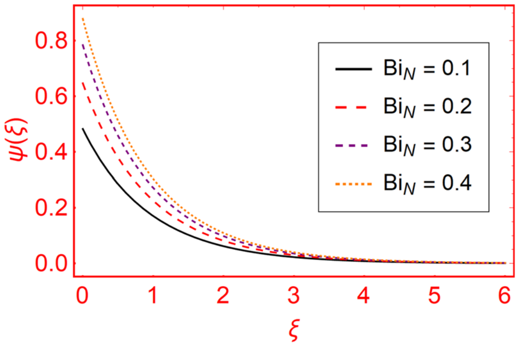

Figure 8: Impact of Bi_N on $\psi(\xi)$.

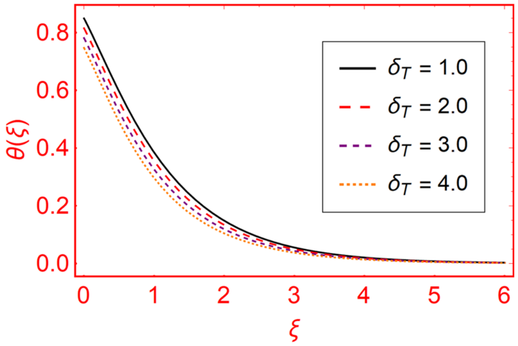

Figure 9: Impact of δ_T on $\theta(\xi)$.

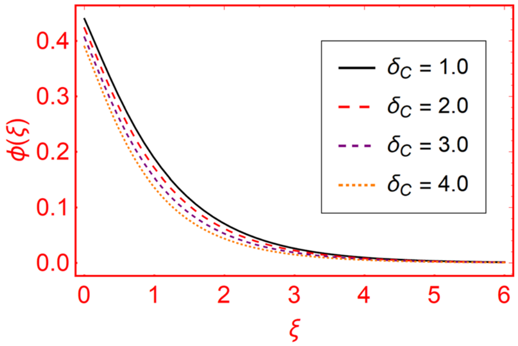

Figure 10: Impact of δ_C on $\phi(\xi)$.

thermal distribution, as shown in Figure 11. Actually, the increase in (Nb) corresponds to a greater random movement of particles within a fluid, which in turn leads to an increase in the thermal distribution. Physically, this means that as (Nb) increases, the individual particles within the fluid experience more frequent collisions and interactions, resulting in greater dispersion of thermal energy throughout the system. Essentially, the particles become more energetic and diffuse more rapidly, contributing to an overall increase in $\theta(\xi)$. This phenomenon has significant implications for various processes, such as heat transfer in colloidal suspensions, where Brownian

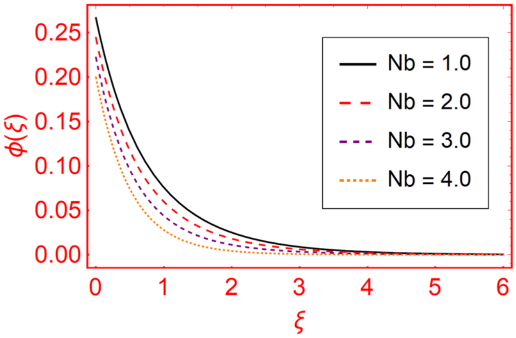

Figure 12: Impact of Nb on $\phi(\xi)$.

motion plays a crucial role in enhancing thermal conductivity and promoting efficient energy transfer. An increase in (Nb) typically corresponds to a decrease in $\phi(\xi)$, as shown in Figure 12. This counterintuitive phenomenon arises from the enhanced random motion of particles within a fluid, which promotes more efficient mixing and diffusion. As Brownian motion intensifies, particles experience greater collisions and erratic movement, leading to greater dispersion throughout the fluid. Consequently, regions of higher concentration become less pronounced as particles spread out more uniformly, while the areas of lower concentration experience influxes of particles due to increased diffusion. This results in a narrowing of concentration gradients and a more homogeneous distribution. This phenomenon has significant implications in various fields, including chemical engineering processes like mixing and dispersion, where understanding the role of Brownian motion is crucial for optimizing performance and product quality. As the thermophoresis factor (Nt) increases, there is a corresponding retardation in the thermal distribution due to the effects of thermophoresis on the particle movement within the fluid, as shown in Figure 13. Physically, thermophoresis refers to the motion of particles induced by temperature gradients, where particles tend to transfer from a zone of higher to lower temperature. When

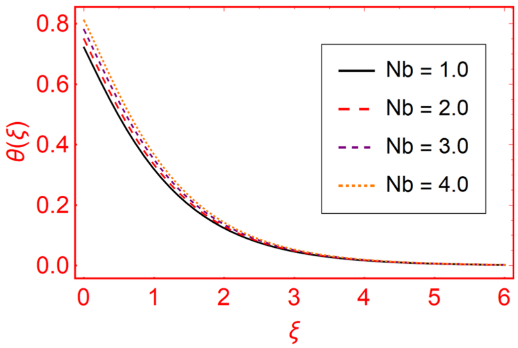

Figure 11: Impact of Nb on $\theta(\xi)$.

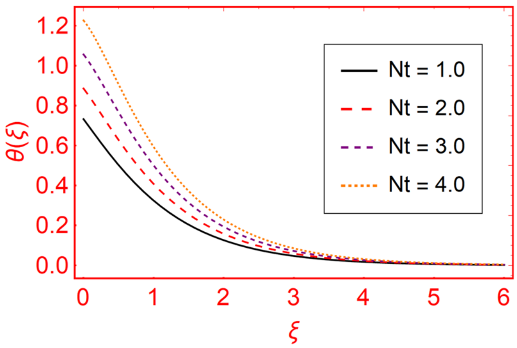

Figure 13: Impact of Nt on $\theta(\xi)$.

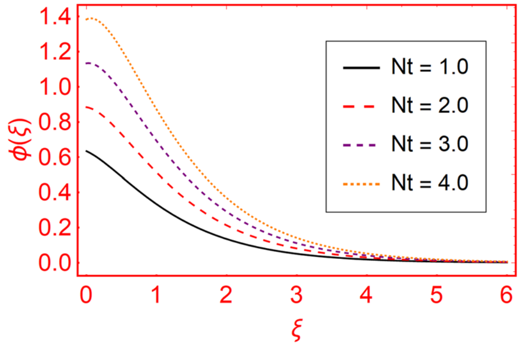

Figure 14: Impact of Nt on $\phi(\xi)$.

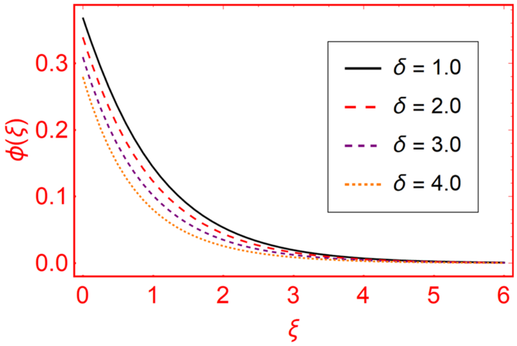

Figure 16: Impact of δ on $\phi(\xi)$.

the thermophoresis factor increases, this migration becomes extra prominent, causing the accumulation of particles in zones of lower temperature. Subsequently, thermal distribution is decreased as the movement of particles tends to counteract the natural heat flow within the system, creating localized deviations from thermal equilibrium. This phenomenon has significant implications in various applications, including combustion processes and aerosol dynamics, where understanding and controlling thermophoresis effects are essential for optimizing thermal management and combustion efficiency. With an increase in the thermophoresis factor (Nt), there is typically an increase in $\phi(\xi)$, as shown in Figure 14 due to the effect of thermophoresis on particle migration within the fluid. When (Nt) increases, it indicates a stronger influence of temperature on the movement of particles. Consequently, this causes more concentration distribution. Essentially, as (Nt) increases, the particles exhibit an increased tendency to migrate toward the regions of differing temperatures, thereby altering the concentration distribution pattern within the fluid. This phenomenon can have significant implications in various fields, like particle transport in biological or industrial processes. Figure 15 shows the influence of radiation factor (Rd) on thermal profiles $\theta(\xi)$. When the radiative factor (Rd) increases, it suggests a larger impact of radiative heat transfer mechanisms within a system. In physical terms, this suggests that more thermal energy is being exchanged within the flow of fluid *via* radiation; consequently, $\theta(\xi)$ increases due to the dispersal of heat throughout the system. Essentially, higher (Rd) leads to more efficient and widespread transfer of thermal energy, resulting in a more uniform thermal distribution across the system. This process is crucial in the processes like heat transfer in engineering systems, atmospheric dynamics, and even in the behavior of celestial bodies where radiation plays a significant role in energy exchange. The effects of variation in the chemical reactivity factor (δ) on $\phi(\xi)$ is shown in Figure 16, where $\phi(\xi)$ decreased with an increase in (δ). Clearly, when (δ) increases, it implies that molecules are more prone to undergo chemical reactions, which often involves the consumption or transformation of reactants into products. This increased reactivity leads to a faster consumption or transformation of the reacting species, thereby causing a decline in $\phi(\xi)$. Physically, this can be interpreted as a scenario where molecules are engaging in reactions more rapidly, depleting their population in the system as they convert into different chemical species. Consequently, the concentration distribution becomes less uniform as reactants are converted into products at a faster rate, altering the overall chemical composition of the

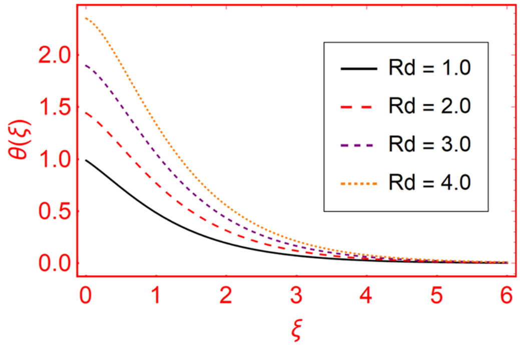

Figure 15: Impact of Rd on $\theta(\xi)$.

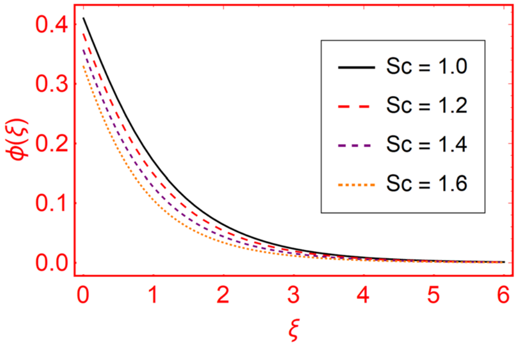

Figure 17: Impact of Sc on $\phi(\xi)$.

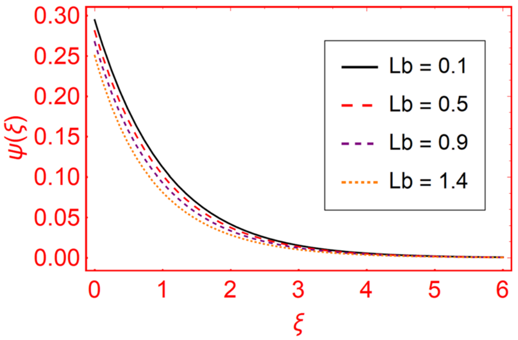

Figure 18: Impact of Lb on $\psi(\xi)$.

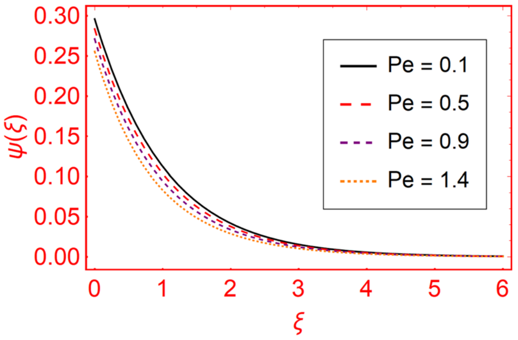

Figure 19: Impact of Pe on $\psi(\xi)$.

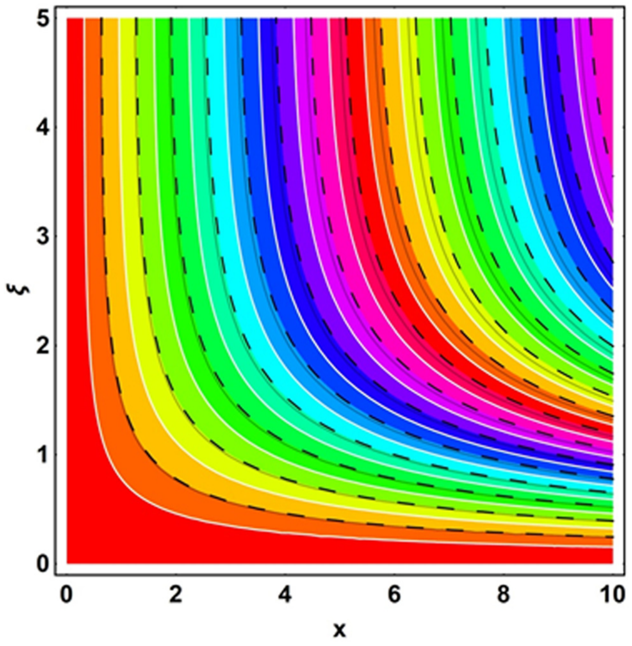

Figure 20: Streamlines behavior of a viscous hybrid nanofluid flow.

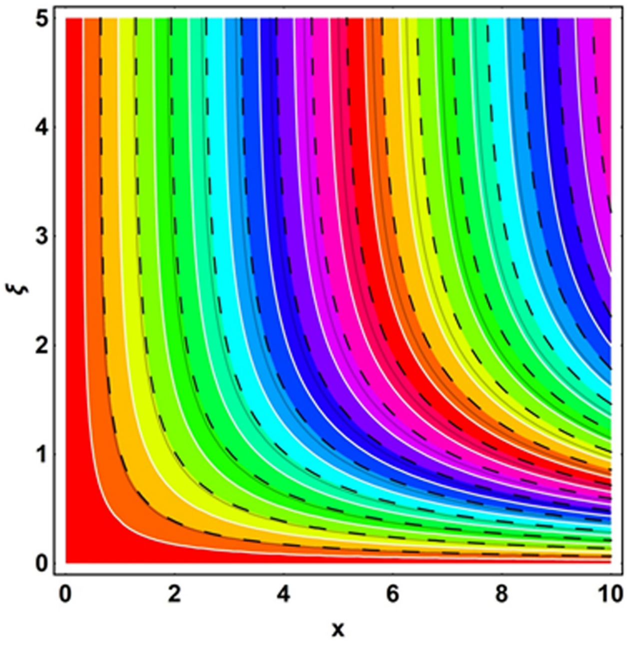

Figure 21: Streamlines behavior of a Carreau–Yasuda hybrid nanofluid flow.

system. The impacts of variation in Schmidt number (Sc) on $\phi(\xi)$ is shown in Figure 17, where $\phi(\xi)$ decreased with an increase in (Sc). When (Sc) increases, it indicates a decrease in the rate of mass transfer relative to the rate of momentum transfer in a fluid system. This means that diffusion becomes less efficient compared to fluid advection, resulting in a slower spread of molecules through the fluid. Consequently, the concentration gradient becomes less pronounced over time, leading to a decline in $\phi(\xi)$. Physically, this can be interpreted as a scenario where the movement of molecules through the fluid is hindered relative to the bulk flow of the fluid itself, causing slower mixing and a reduction in the overall uniformity of concentration within the system. The impacts of variation in bio-convection Lewis number (Lb) on $\psi(\xi)$ is shown in Figure 18, where $\phi(\xi)$ decreases with an increase in (Lb). Increase in (Lb) suggests that the diffusivity of nutrients as well as other substances essential for microbial growth relative to the diffusivity of momentum in the fluid decreases. This implies that the transport of nutrients becomes less efficient compared to the movement of the surrounding fluid. As a

Table 6: Impacts of M and We on C_{f}

M	We	C_{f}
0.1		1.446446
0.2		1.497544
0.3		1.529986
	0.1	1.475363
	0.2	1.486436
	0.3	1.497535

result, microorganisms experience decreased access to essential nutrients required for their growth and proliferation. Physically, this can be interpreted as a scenario where the nutrient gradients in the fluid become less pronounced, decreasing the ability of microorganisms to efficiently acquire nutrients from their surroundings. Consequently, there is a decline in the distribution and abundance of microorganisms as their growth is limited by nutrient availability in the environment. The impacts of variation in Peclet number (Pe) on $\psi(\xi)$ is shown in Figure 19, where $\phi(\xi)$ decreases with an increase in (Pe). The increase in (Pe) suggests a domination of convective transportation over diffusive transportation in the fluid flow on a surface. This implies that the fluid velocity becomes more significant compared to molecular diffusion in transporting nutrients and other substances. As a result, microorganisms experience less time to interact with the surface, leading to reduced attachment and colonization. Essentially, the higher Peclet number accelerates the fluid flow, diminishing the residence time of microorganisms near the surface, thereby decreasing their profiles and potentially impacting processes like biofilm formation or microbial activity. Figures 20 and 21 show the streamlines performance of a viscous hybrid nanofluid flow and Carreau increase Yasuda hybrid nanofluid flow. From these figures, a clear difference between the behavior of a viscous hybrid nanofluid flow and Carreau–Yasuda hybrid nanofluid flow is obtained. Table 6 shows the influence of M and We on C_{f}. A higher M and We enhances C_{f}, as shown in Table 6. The reason is that the greater values of M yields the Lorentz forces that always acts in a reverse direction of fluid motion. This opposition is due to the greater friction force at sheet's surface. Also, the higher values of We enhances C_{f}. Table 7 shows the influences of Rd, δ_{T}, Nt, and Nb on N_{u}. The higher values of Rd and Nt enhance N_{u} while the higher values of δ_{T} and Nb decreases N_{u}.

Table 7: Impacts of Rd, δ_{T}, Nt and Nb on N_{u}

Rd	δ_{T}	Nt	Nb	N_{u}
0.1				1.964367
0.2				1.975374
0.3				1.986363
	0.1			1.753253
	0.2			1.732135
	0.3			1.718437
		0.1		1.753568
		0.2		1.798543
		0.3		1.833684
			0.1	1.987543
			0.2	1.959224
			0.3	1.924684

7 Conclusions

This study examines a time-independent and incompressible blood-based hybrid nanofluid flow containing Cu and Au nanoparticles on elongating surfaces. A non-Newtonian model called Carreau–Yasuda was used with effects of thermal radiation, magnetic field, Brownian motion, thermophoresis, and chemical reactivity. The main equations were evaluated through HAM. The convergence analysis of HAM was investigated, and the HAM and numerical analyses were compared. Based on the above assumptions, the following concluding points are obtained:

- It was found that increasing the magnetic factor decreases the velocity profile while the higher Weissenberg number increases the velocity profile.
- The higher thermal, concentration, and microorganism Biot numbers increased the thermal, concentration, and microorganism profiles, respectively.
- The greater thermal and concentration relaxation time factors decreased the thermal and concentration panels, respectively.
- The greater Brownian motion factor increased the thermal panels while it decreased the concentration panels.
- The greater thermophoresis factor increased both the thermal and concentration panels.
- The higher Schmidt number and chemical reactivity factor decreased the concentration profiles.
- The higher bioconvection Lewis and Peclet numbers decreased the microorganism profiles.
- The increasing magnetic factor and Weissenberg number increased the skin friction at the sheet surface.
- Both the HAM and numerical methods solved the modeled equations, which validated both the solution methodologies.

8 Future recommendations

In the future, this study will be associated with a three-dimensional blood-based hybrid nanofluid flow containing Cu and Au nanoparticles on elongating surfaces. Also, different metallic and non-metallic nanomaterials can be considered to investigate the same model by considering different physical conditions like first- and second-order velocity slip, thermal slip, mass flux, and zero-mass flux constraints.

Acknowledgments: The authors acknowledge the Princess Nourah bint Abdulrahman University Researchers Supporting Project number (PNURSP2024R443), Princess Nourah bint Abdulrahman University, Riyadh, Saudi Arabia. This work was supported by the Deanship of Scientific Research, the Vice Presidency for Graduate Studies and Scientific Research, King Faisal University, Saudi Arabia (GrantA153).

Funding information: Princess Nourah bint Abdulrahman University Researchers Supporting Project number (PNURSP2024R443), Princess Nourah bint Abdulrahman University, Riyadh, Saudi Arabia. This work was supported by the Deanship of Scientific Research, the Vice Presidency for Graduate Studies and Scientific Research, King Faisal University, Saudi Arabia (GrantA153).

Author contributions: All authors have accepted responsibility for the entire content of this manuscript and approved its submission.

Conflict of interest: The authors state no conflict of interest.

Data availability statement: All data generated or analyzed during this study are included in this published article.

References

[1] Pandey S, Yoon SY, Balachandar S, Ha MY. Experimental and numerical investigations of thermal and flow characteristics of a shear-thinning non-Newtonian fluid in a differentially heated cavity. Int J Heat Mass Transf. 2022;187:122570.

[2] Xu Y, Rao S, Wendi Y, Junchao Y, Liu F, Cheng GJ. Revolutionizing protective materials: Ultrahigh peak viscosity through MOF-enhanced shear thickening fluid for advanced soft body armor. Appl Mater Today. 2024;37:102126.

[3] Asghar Z, Khan MWS, Pasha AA, Rahman MM, Sankaralingam L, Alam MI. On non-Newtonian fluid flow generated *via* complex metachronal waves of cilia with magnetic, hall, and porous effects. Phys Fluids. 2023;35.

[4] Pasha AA, Alam MM, Tayebi T, Kasim S, Dogonchi AS, Irshad K, et al. Heat transfer and irreversibility evaluation of non-Newtonian nanofluid density-driven convection within a hexagonal-shaped domain influenced by an inclined magnetic field. Case Stud. Therm Eng. 2023;41:102588.

[5] Punith Gowda RJ, Sarris IE, Naveen Kumar R, Kumar R, Prasannakumara BC. A three-dimensional non-newtonian magnetic fluid flow induced due to stretching of the flat surface with chemical reaction. J Heat Transf. 2022;144:113602.

[6] Nazeer M, Alqarni MZ, Hussain F, Saleem S. Computational analysis of multiphase flow of non-Newtonian fluid through inclined channel: heat transfer analysis with perturbation method. Comput Part Mech. 2023;10:1–11.

[7] Ragupathi E, Prakash D. Role of linear and nonlinear thermal radiation over the rotating porous disc with the occurrence of non-uniform heat source/sink: HAM analysis. Math Comput Simul. 2023.

[8] Biswal MM, Swain K, Dash GC, Ojha K. Study of radiative magneto-non-Newtonian fluid flow over a nonlinearly elongating sheet with Soret and Dufour effects. Numer Heat Transf Part A Appl. 2023;83:331–42.

[9] Choi SUS, Eastman JA. Enhancing thermal conductivity of fluids with nanoparticles. 1995 Int Mech Eng Congr Exhib San Fr CA (United States), 12–17 Nov 1995 [Internet]; 1995 [cited 2021 Oct 2]. https://digital.library.unt.edu/ark:/67531/metadc671104/.

[10] Yasmin H, Akram S, Athar M, Saeed K, Razia A, Al-Juaid JG. Impact of multiple slips on thermally radiative peristaltic transport of Sisko nanofluid with double diffusion convection, viscous dissipation, and induced magnetic field. Nanotechnol Rev. 2024;13:20240004.

[11] Bhatti MM, Vafai K, Abdelsalam SI. The role of nanofluids in renewable energy engineering. Nanomaterials. MDPI; 2023. p. 2671.

[12] Abdelsalam SI, Zaher AZ. Biomimetic amelioration of zirconium nanoparticles on a rigid substrate over viscous slime – a physiological approach. Appl Math Mech. 2023;44:1563–76.

[13] Acharya N, Mabood F, Shahzad SA, Badruddin IA. Hydrothermal variations of radiative nanofluid flow by the influence of nanoparticles diameter and nanolayer. Int Commun Heat Mass Transf. 2022;130:105781.

[14] Abdelsalam SI, Alsharif AM, Abd Elmaboud Y, Abdellateef AI. Assorted kerosene-based nanofluid across a dual-zone vertical annulus with electroosmosis. Heliyon. 2023;9:15916.

[15] Khalil S, Yasmin H, Abbas T, Muhammad T. Analysis of thermal conductivity variation in magneto-hybrid nanofluids flow through porous medium with variable viscosity and slip boundary. Case Stud Therm Eng. 2024;57:104314.

[16] Abdelsalam SI, Bhatti MM. Unraveling the nature of nano-diamonds and silica in a catheterized tapered artery: highlights into hydrophilic traits. Sci Rep. 2023;13:5684.

[17] Alshehry AS, Yasmin H, Ganie AH, Shah R. Heat transfer performance of magnetohydrodynamic multiphase nanofluid flow of $Cu–Al_2O_3/H_2O$ over a stretching cylinder. Open Phys. 2023;21:20230142.

[18] Raizah Z, Khan A, Gul T, Saeed A, Bonyah E, Galal AM. Coupled Dufour and Soret effects on hybrid nanofluid flow through gyrating channel subject to chemically reactive Arrhenius activation energy. J Nanomater. 2023;2023:1–13.

[19] Mahabaleshwar US, Maranna T, Pérez LM, Ravichandra Nayakar SN. An effect of magnetohydrodynamic and radiation on axisymmetric flow of non-Newtonian fluid past a porous shrinking/stretching surface. J Magn Magn Mater. 2023;571:170538.

[20] Prakash D, Suriyakumar P, Sivakumar N, Kumar BR. Influence of viscous and Ohmic heating on MHD flow of nanofluid over an inclined nonlinear stretching sheet embedded in a porous medium. Int J Mech Eng Technol. 2018;9:992–1001.

[21] Goud BS, Srilatha P, Mahendar D, Srinivasulu T, Dharmendar Reddy Y. Thermal radiation effect on thermostatically stratified MHD fluid flow through an accelerated vertical porous plate with viscous dissipation impact. Partial Differ Equ Appl Math. 2023;7:100488.

[22] Patel H, Mittal A, Nagar T. Fractional order simulation for unsteady MHD nanofluid flow in porous medium with Soret and heat generation effects. Heat Transf. 2023;52:563–84.

[23] Mahesh R, Mahabaleshwar US, Kumar PNV, Öztop HF, Abu-Hamdeh N. Impact of radiation on the MHD couple stress hybrid nanofluid flow over a porous sheet with viscous dissipation. Results Eng. 2023;17:100905.

[24] Jawad M. A computational study on magnetohydrodynamics stagnation point flow of micropolar fluids with buoyancy and thermal radiation due to a vertical stretching surface. J Nanofluids. 2023;12:759–66.

[25] Lund LA, Yashkun U, Shah NA. Magnetohydrodynamics streamwise and cross flow of hybrid nanofluid along the viscous dissipation effect: Duality and stability. Phys Fluids. 2023;35.

[26] Algehyne EA, Alhusayni YY, Tassaddiq A, Saeed A, Bilal M. The study of nanofluid flow with motile microorganism and thermal slip condition across a vertical permeable surface. Waves Random Complex Media. 2022;1–18.

[27] Kada B, Hussain I, Ali Pasha A, Azeem Khan W, Tabrez M, Juhany KA, et al. Significance of gyrotactic microorganism and bioconvection analysis for radiative Williamson fluid flow with ferromagnetic nanoparticles. Therm Sci Eng Prog. 2023;39:101732.

[28] Li G, Gong Z, Jiang W, Zhan J, Wang B, Fu X, et al. Environmental transport of gyrotactic microorganisms in an open-channel flow. Water Resour Res. 2023;59:e2022WR033229.

[29] Doh DH, Muthtamilselvan M, Prakash D. Transient heat and mass transfer of micropolar fluid between porous vertical channel with boundary conditions of third kind. Int J Nonlinear Sci Numer Simul. 2016;17:231–42.

[30] Khan A, Saeed A, Tassaddiq A, Gul T, Kumam P, Ali I, et al. Bio-convective and chemically reactive hybrid nanofluid flow upon a thin stirring needle with viscous dissipation. Sci Rep. 2021;11:1–17.

[31] Waqas M, Khan WA, Pasha AA, Islam N, Rahman MM. Dynamics of bioconvective Casson nanoliquid from a moving surface capturing gyrotactic microorganisms, magnetohydrodynamics and stratifications. Therm Sci Eng Prog. 2022;36:101492.

[32] Fourier JBJ. Théorie analytique de la chaleur. Gauthier-Villars et fils; 1888.

[33] Fick A. On liquid diffusion. J Memb Sci. 1995;100:33–8.

[34] Cattaneo C. Sulla conduzione del calore. Atti Sem Mat Fis Univ Modena. 1948;3:83–101.

[35] Christov CI. On frame indifferent formulation of the Maxwell–Cattaneo model of finite-speed heat conduction. Mech Res Commun. 2009;36:481–6.

[36] Waqas H, Farooq U, Liu D, Imran M, Muhammad T, Alshomrani AS, et al. Comparative analysis of hybrid nanofluids with Cattaneo-Christov heat flux model: A thermal case study. Case Stud Therm Eng. 2022;36:102212.

[37] Saleem M, Tufail MN. Analysis of the unsteady upper-convected Maxwell fluid having a Cattaneo–Christov heat flux model *via* two-parameters Lie transformations. Indian J Phys. 2023;1–11.

[38] Saraswathy M, Prakash D, Muthtamilselvan M, Al-Mdallal QM. Theoretical study on bio-convection of micropolar fluid with an exploration of Cattaneo–Christov heat flux theory. Int J Mod Phys B. 2024;38:2450016.

[39] Waqas H, Fida M, Liu D, Manzoor U, Muhammad T. Numerical simulation of entropy generation for nanofluid with the consequences of thermal radiation and Cattaneo-Christov heat flux model. Int Commun Heat Mass Transf. 2022;137:106293.

[40] Ramesh D, Babu MM, Prakash GB, Rani KJ, Praveen JP, Reddy GV. Magnetohydrodynamic effects on heat and mass transfer in hybrid nanofluid flow over a stretched sheet with Cattaneo-Christov model. CFD Lett. 2024;16:105–17.

[41] Ramzan M, Javed M, Rehman S, Ahmed D, Saeed A, Kumam P. Computational assessment of microrotation and buoyancy effects on the stagnation point flow of carreau–yasuda hybrid nanofluid with chemical reaction past a convectively heated riga plate. ACS Omega. 2022;7:30297–12.

[42] Dawar A, Islam S, Shah Z, Mahmuod SR. A passive control of Casson hybrid nanofluid flow over a curved surface with alumina and copper nanomaterials: a study on sodium alginate-based fluid. J Mol Liq. 2023;382:122018.

[43] Das S, Pal TK, Jana RN, Giri B. Ascendancy of electromagnetic force and Hall currents on blood flow carrying Cu-Au NPs in a non-uniform endoscopic annulus having wall slip. Microvasc Res. 2021;138:104191.